Title
A Novel Structure of Intercalated Graphene in Quantum Dot Films for Improved Light Absorption and Enhanced Charge Extraction

Permalink
https://escholarship.org/uc/item/3gm80490

Author
Chen, Wenjun

Publication Date
2019

UNIVERSITY OF CALIFORNIA SAN DIEGO

A Novel Structure of Intercalated Graphene in Quantum Dot Films for Improved Light Absorption and Enhanced Charge Extraction

A dissertation submitted in partial satisfaction of the
requirements for the degree Doctor of Philosophy

in

Materials Science and Engineering

by

Wenjun Chen

Committee in charge:

Professor Oscar Vazquez-Mena, Chair
Professor Prabhakar Bandaru
Professor Ertugrul Cubukcu
Professor David Fenning
Professor Donald Sirbuly

2019

The Dissertation of Wenjun Chen is approved, and it is acceptable in quality and form for publication on microfilm and electronically:

Chair

University of California San Diego

2019

DEDICATION

To my parents

TABLE OF CONTENTS

LIST OF FIGURES

LIST OF TABLES

ACKNOWLEDGEMENTS

First of all, I would like to sincerely thank my advisor Professor Oscar Vazquez-Mena. Without his constant guidance over the years, this work would not be achieved successfully. I was inspired and enlightened by his intelligence, profound knowledge, acute insights, deep understanding of the philosophy of research, sense of humor and most importantly, passion for science.

I would like to thank my dissertation committee, Professor David Fenning, he has provided valuable suggestions about the device analysis and help with quantum efficiency measurement. I also would like to thank Professor Prabhakar Bandaru, Professor Ertugrul Cubukcu and Professor Donald Sirbuly, for their time, insightful comments and constructive guidance that significantly improved this dissertation.

I also would like to express my appreciation to my previous and current labmates and colleagues at UC San Diego. Mr. Seungbae Ahn, Mr. Jiaying Wang, Mr. Malcolm Lockett, Mr. Joshua Castro, Mr. Marquez Balingit, Mr. Carlos Rangel, and Ms. Xiaochen Li thanks for their collaborations and helps during the past four years.

The collaborations with Lucia Curri and Chiara Ingrosso from Italian National Research Council are certainly memorable. The help of PL measurement from Dr. Athena Pan and Professor Shaya Fainman is also appreciated.

The support from National Science Foundation Award No. 1710472 is gratefully acknowledged. I also would like to thank the fellowship award from UCSD, financial support and training from being research and teaching assistant at UCSD.

Last but not least I want to express my gratitude to my parents. Both of them did their best to offer me a pleasant growing environment, raising me into an adult with a sense of responsibility, an optimistic spirit and grateful attitude for appreciation of life. I am especially grateful to their support for my study abroad, both emotionally and financially. They are always being a constant source of love and support for me. I also would like to thank Alex for his encouragement and moral support during the past five years, thanks for his constantly encouraging me in all of my pursuits and inspiring me to follow my dreams.

Chapter 2, in full, is a reprint of the material as it appears in “Improved Charge Extraction Beyond Diffusion Length by Layer-by-Layer Multistacking Intercalation of Graphene Layers inside Quantum Dots Films”. Chen, Wenjun; Castro, Joshua; Ahn, Seungbae; Xiaochen Li; Vazquez-Mena, Oscar. Advanced Materials, 31, 1-6 (2019). The dissertation author was the primary investigator and author of this paper.

Chapter 3, in full, is a reprint of the material as it appears in “Implementation of Metallic Vertical Interconnect Access in Hybrid Intercalated Graphene/Quantum Dot Photodetector for Improved Charge Collection”. Chen, Wenjun; Ahn, Seungbae; Rangel, Carlos; Vazquez-Mena, Oscar. Frontiers in Materials. 6, 1-7 (2019). The dissertation author was the primary investigator and author of this paper.

Chapter 4, in full, is a reprint of the material as it appears in “Near Full Light Absorption and Full Charge Collection in 1-micron Thick Quantum Dot Photodetector Using Intercalated Graphene Monolayer Electrodes” Chen, Wenjun; Ahn, Seungbae; Balingit, Marquez; Wang, Jiaying; Lockett, Malcolm: Vazquez-Mena, Oscar. Submitted. The dissertation author was the primary investigator and author of this paper.

VITA

EDUCATION:

University of California, San Diego Sep. 2015 – Dec. 2019

- Ph.D in Materials Science and Engineering, GPA 3.8/4.0

University of California, Merced Sep. 2013 - May. 2015

- M.S. in Mechanical Engineering, GPA 4.0/4.0

Dalian University of Technology, China Sep. 2009 - Jul. 2013

- B.S. degree in Materials Processing and Control Engineering, GPA 3.67/4.0

RESEARCH EXPERIENCE

Graduate Researcher

Oscar Vazquez-Mena Lab, *University of California, San Diego* Sep. 2015 - Present

Quantum Dot Photodetector Devices Research Project

- Studied PbS quantum dots and graphene properties, quantum dots film formation and graphene film transfer.
- Intercalated graphene for enhanced charge extraction and light absorption in photodetection devices.
- Utilizing nanofabrication techniques, such as photolithography, e-beam evaporate, plasma etching, to achieve an intercalated graphene and quantum dots hybrid photodetector devices with enhanced charge extraction and ultra-high responsivity.
- XRD, SEM, Raman, XPS, PL, EQE and other electrical characteristic measurements to analyze devices.

Graduate Researcher

Vincent C.Tung Lab, *University of California, Merced* Jan. 2014 - May. 2015

Crumpled Graphene Research Project

- Created graphene oxide crumples through electrospraying technique and graphene oxide surface modification for energy harvesting.
- Utilized co-axial electrospraying system of self-assembly graphitic materials such as carbon nanotubes (CNTs) and C_{60} on flexible substrates for photovoltaic applications.

Perovskite Solar Cell Research Project

- Investigated perovskite thin film deposition by electrospraying bi-solvent system precursor and post-annealing treatment for optimizing the film morphology.

Bachelor's Thesis, *Dalian University of Technology, China* 2012 – 2013

High-entropy Alloy Thin Film Project

- Studied the magnetron sputtering deposition of WVNbZrMoTi high-entropy alloy thin film, designed the equimolar mosaic target, as well as the composition, microstructure and mechanical properties.
- Achieved high-entropy thin film with high hardness and elastic modulus.

Competition Candidate, *Dalian University of Technology, China* 2011

YongGuan Cup Casting Competition

- Completed the analysis of castings, design of the gating system and sand core box, and finished the whole casting design by computer-aided simulation. Won the excellent award.

Undergraduate Researcher, *Dalian University of Technology, China* 2010 - 2012

National University Students Innovation Experimental Project

- Used TIG method to weld aluminum alloy and stainless steel with an additional transition metal layer on the stainless steel, to avoid the nonhomogeneous stress distribution caused by different thermal expansion coefficient and low solid solubility.

PROFESSIONAL EXPERIENCE

University of California, San Diego Winter 2017/2018/2019

- Teaching Assistant for Introduction to Nanoengineering

University of California, Merced 2013/2014/2015

- Teaching Assistant
    - Statics and Dynamics, Heat Transfer, Pro-Engineering, Matlab, Fortran

Intern, FAW Automobile Co., Ltd, **China** Jul. 2012 – Sep. 2012

- Compression modeling of the automobile side doors and post thermal treatment

Intern, Chemical Fiber Group Co., Ltd, China Jul. 2010 – Aug. 2010

- Analysis of the properties of viscose filament yarn

PATENT

Intercalated Graphene Layers for Charge Extraction, U.S. Patent Application No. 16/016,407.

PUBLICATION

- Chen, W.; Ahn, S.; Rangel, C.; Vazquez-Mena, O. Implementation of Metallic Vertical Interconnect Access in Hybrid Intercalated Graphene/Quantum Dot Photodetector for Improved Charge Collection. *Front. Mater.* **2019**, *6*, 1–7.
- Chen, W.; Castro, J.; Ahn, S.; Li, X.; Vazquez-Mena, O. Improved Charge Extraction Beyond Diffusion Length by Layer-by-Layer Multistacking Intercalation of Graphene Layers inside Quantum Dots Films. *Adv. Mater.* **2019**, *31*, 1–6.
- Sarmiento, V.; Lockett, M.; Chen, W.; Ahn, S.; Wang, J.; Vazquez-mena, O.; Diego, C. S.; Jolla, L.; Diego, S. Electrochemical Functionalization Strategy for CVD Graphene on Silicon Substrates : Grafting , Electronic Properties and Biosensing. *Nanotechnology* **2019**.
- Wang, J.; Wagner, S.; Chen, W.; Shi, Y.; Ndao, A.; Li, L.; Kante, B.; Sirbuly, D.; Lemme, M. C.; Vazquez-Mena, O. Integration of Nanomaterials into Three-Dimensional Vertical Architectures. *ACS Appl. Mater. Interfaces* **2018**, *10*, 28262–28268.
- Ishihara, H.; Chen, W.; Chen, Y. C.; Sarang, S.; De Marco, N.; Lin, O.; Ghosh, S.; Tung, V. Electrohydrodynamically Assisted Deposition of Efficient Perovskite Photovoltaics. *Adv. Mater. Interfaces* **2016**, *3*, 1–11.
- Chen, Y. C.; Ishihara, H.; Chen, W. J.; Demarco, N.; Siordia, A.; Sun, Y.; Lin, O.; Chu, C. W.; Tung, V. C. Capillarity-Assisted Electrostatic Assembly of Hierarchically Functional 3D Graphene: TiO2Hybrid Photoanodes. *Adv. Mater. Interfaces* **2015**, *2*, 1–7.

HONORS, AWARDS AND SCHOLORSHIP

• Fellowship	**2015**
• Academic Scholarship	**2012/2011/2010**
• Dean’s Honor list	**2012/2011/2010**
• Fu Gang Scholarship	**2010**
• Sport and Art Scholarship	**2010**
• Merit Student	**2010**

SKILLS

Programming languages and software

- Matlab
- ProCAST
- LaTex
- Illustrator
- AutoCAD
- C++
- Fortran
- Origin

Laboratory skills

- Photolithography
- UV-Vis spectroscopy
- Thin film deposition
- SEM
- TEM
- Spin coating
- Graphene transfer
- Dry etch
- XRD
- Raman Spectroscopy

ABSTRACT OF THE DISSERTATION

A Novel Structure of Intercalated Graphene in Quantum Dot Films for Improved Light Absorption and Enhanced Charge Extraction

by

Wenjun Chen

Doctor of Philosophy in Materials Science and Engineering

University of California San Diego, 2019

Professor Oscar Vazquez-Mena, Chair

PbS quantum dots (QDs) are promising materials for optoelectronic devices due to their size-tunable band gap, strong light absorption and low cost solution processing.[1,2] However, efficient charge collection is a major issue for QDs films due to the poor film mobility and short diffusion length (~200 nm). If QDs film thickness is beyond diffusion length, electron and hole pair generation occurs too far from the junction, charge carriers will recombine before producing any photocurrent. Thus, there is a compromise of QDs thickness between efficient charge extraction and light absorption, the thickness of absorbing layers should not exceed the carrier

diffusion length plus depletion width. This has restricted the practical QDs film thickness to ~200-300 nm due to the limitation that the diffusion length imposes on film thickness in order to keep efficient charge collection. Such thin films result in a significant decrease in quantum efficiency for λ>700 nm in QDs optoelectronic devices, causing a reduced photoresponsivity and a poor absorption towards the infrared part of the sunlight spectrum, wasting almost half of solar energy.

In this work, we present a novel architecture that incorporates multiple intercalated graphene layers inside the QD film to enhance charge extraction, breaking the restriction that short diffusion length imposes on the QDs film thickness. The intercalated graphene layers ensure a faster and more efficient carrier collection to enhance the performance while increasing the QDs film thickness, especially in the near-infrared range. The intercalated Gr/QD devices were made by sequential Gr wet transfer and QD spin coating on SiO_2/Si substrate with predefined gold electrodes. The intercalating graphene layers ensure the efficient charge extraction despite the thickness increment, breaking the limitation that diffusion length imposes on QDs film thickness. We also added the vertical interconnect access between each graphene layers by depositing Au electrodes on each graphene with E-beam evaporator and shadow mask. Furthermore, the optimal graphene interspace, which is the QDs film thickness between two graphene layers, is studied to ensure the efficient charge extraction as well as fabrication efficiency. At last, we fabricated 1-miron meter thick device by employing this intercalated Gr/QD configuration.

We demonstrate high quantum efficiency (~90% to 70%) from λ = 600 nm to 950 nm with this 1-miron meter thick Gr/QDs device, avoiding the drastic drop at λ =700 nm. We achieved device photoresponsivity of 10^7AW^{-1}, indicating corresponding gains of 10^8. We also demonstrate this technology is flexible substrate compatible, showing 70% of the original performance after 1000 times bending test on flexible PET substrate. This work demonstrates the first intercalated

Gr/QD hybrid photodetectors, introducing a new approach to achieve high light absorption and efficient charge collection in high-response photodetectors. Our approach allows breaking the restriction that diffusion length imposes on the thickness of QD layers and paves the way for the development of multi-band photodetector, high efficiency photovoltaics, high resolution CMOS camera, as well as wearable sensors.

Chapter 1 Introduction

1.1 Background

Colloidal quantum dots (QDs) are solution-processing semiconductors of great interests in optoelectronic devices with low-cost fabrication and high efficiency performance simultaneously.[3] The unique size-, shape-, and composition-tunable electronic and optical properties make QDs attractive for enabling customization of photodetectors and photovoltaics absorption profile to harvest the solar energy.

1.1.1 Quantum Dots and Optoelectronic Properties

QDs are nanoscale crystals of analogous bulk semiconductor crystals, typically with sizes less than 10nm.[4] In this size range, quantum confinement effects make QDs can be tailored in size, shape and composition, and allowing QDs possess unique size, shape, and composition dependent electronic and optical properties.[4],[5] In addition, the large surface-to-volume ratio plays an important role in electrical properties, such as the concentration, motion, and dynamics of excitons and charge carriers in QD solids. Long-chain organic ligands stabilized CQDs can be prepared with controlled nanoparticle crystallinity and size in well-established synthetic methods.[6] Exchange to shorter ligands has been well studied and employed to have enhanced charge carrier mobility and other electronic properties.[6–11]

Among the QDs demonstrated to date, lead salt QDs (PbX, X = S, Se, Te) have drawn special attentions world widely as promising candidates for optoelectronic devices in past decades.[12] Lead salt QDs can be size-tuned to absorb light strongly in the infrared (IR) and near-infrared (NIR) spectrum range, which is a significant wavelength region for solar energy harvesting.[12] In contrast with II-VI and III-V QDs, lead salt QDs are investigated to have strong quantum confinement effects due to relatively small electron and hole masses and large Bohr radii,[13] resulting in the electron (hole) wavefunction extending beyond the physical boundary of lead salt QDs. Correspondingly lead salt QDs end up with strong electronic coupling to a neighboring dot or other electron/hole conductors, thus high conductivity and charge carrier mobility,[12],[13] which are properties of significance in solar cells and photodetectors.

The critical parameters of QDs that play an important role in optoelectronic devices are carrier mobility, doping density, trap density, and diffusion length in films (Table 1.1).[14] These parameters will be discussed in this section.

Table 1.1 Common quantum dot film optoelectronic parameters[14]

Property	Related Solar Cell Parameters	Testing Method
Carrier mobility	J_{sc}, FF	CELIV, TOF, J_{sc} transient decay
Trap density	V_{oc}, J_{sc}, FF	V_{oc} transient decay
Doping density	V_{oc}, FF	Capacitance-voltage, FET
Carrier lifetime	J_{sc}, FF	V_{oc} transient decay
Diffusion length	J_{sc}, FF	Photoluminescence quenching

J_{sc} = short-circuit current, V_{oc} = open-circuit voltage, FF = fill factor, CELIV= carrier extraction by linearly increasing voltage, TOF = time of flight, and FET = field effect transistor.

Carrier mobility is a measure of the speed of a charge carrier as it moves through a conductive medium with the presence of an electric field.[15] Electrons and holes move at the thermal velocity in random directions under no-electrical filed condition, their directions of motion change frequently due to collisions or scattering with imperfections in the crystal. When a voltage is applied to a semiconductor device, charge carriers would be in drift mode caused by the electric field, and the drift velocity is superimposed on the thermal motion. Consider the case for holes, the mean free time between collisions is τ_{mp} and the carrier loses its entire drift momentum, $m_p v$, after each collision. And the drift momentum gained between each collision equal to the force, $q\xi$, times the mean time for momentum relaxation (Equation1.1). The proportionality constant μ_p is the hole mobility, the electron mobility can be achieved in similar way. A faster charge carrier mobility is desired for faster operated devices, thus carrier mobility is one of the most important parameters for semiconductors and is of significance for QDs photovoltaic devices.

$$m_p v = q\xi\tau_{mp}$$
$$v = \frac{q\xi\tau_{mp}}{m_p}$$
$$v = \mu_p \xi$$
$$\mu_p = \frac{q\tau_{mp}}{m_p} \qquad \text{Equation 1.1}$$

Carrier mobility can be extracted by using the method of carrier extraction by linearly increasing voltage (CELIV),[16,17] a series of characterizations of PbS QDs electronic properties was studied.[17] They applied a linearly increasing voltage to various photovoltaic devices (300-600 nm thick) in reverse bias and monitored the current signal through a 50 Ω load.[17] **Figure 1.1 a** shows a representative CELIV transient curve (at ramp rate of 80 000Vs^{-1}).[17] The majority carrier mobility (hole mobility for a p-type semiconductor) can be calculated from the time required for the transient current to reach the maximum value. And the extracted hole mobility (μ_p) was (1.5 ± 0.1) × 10^{-3} cm^{2}V^{-1}s^{-1}. The minority mobility was obtained by using time-of-flight (TOF) method in optically thick films and the transient curve is presented in **Figure 1.1 b**. In order to ensure the accurate measurement, the film thickness is typically required to exceed 1 μm, to avoid the resistive-capacitive-delay-limited, and in that case the transient time is observable.[14] The minority mobility (μ_e) was found to be (2 ± 1) × 10^{-4} cm^{2}V^{-1}s^{-1}, which is one order of magnitude lower than majority carrier mobility.[17]

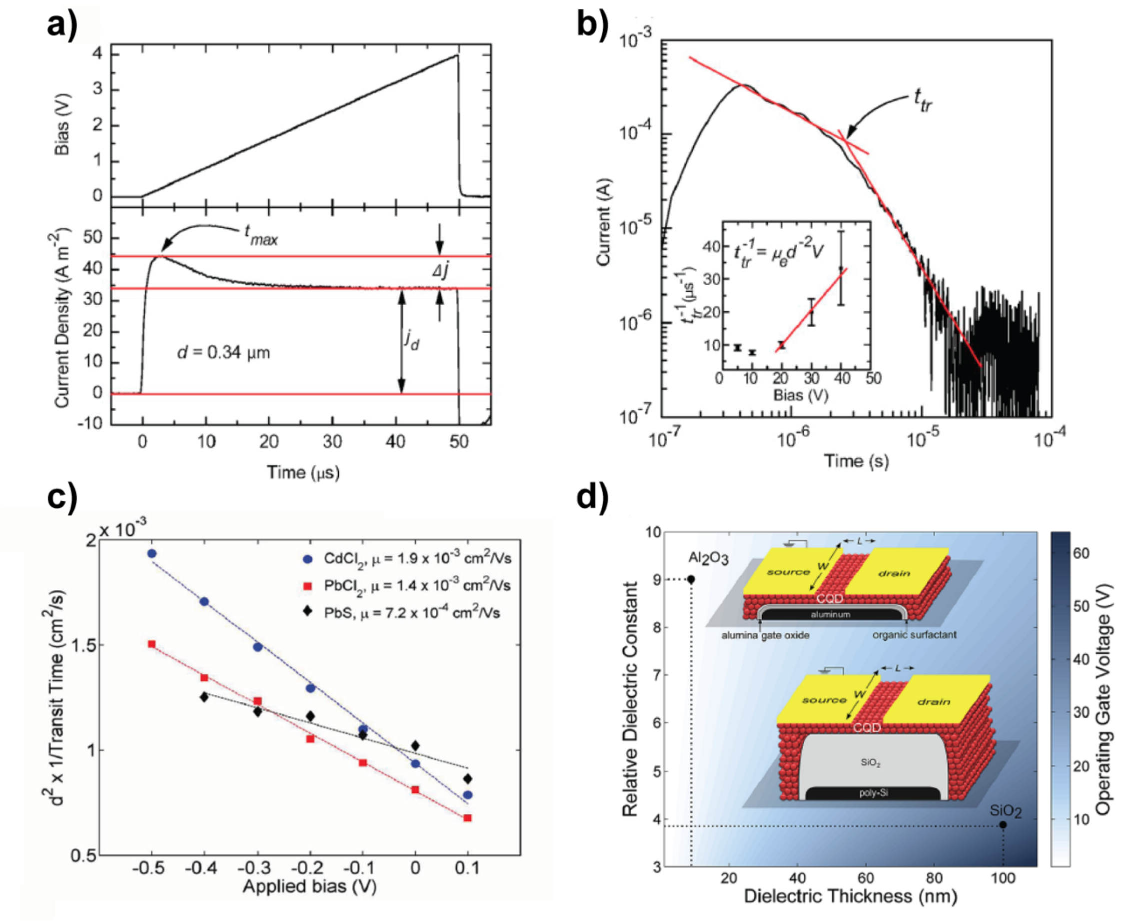

Figure 1.1 Recent development of methods for carrier mobility measurement. Representative current transient signals used to extract a) the hole mobility (CELIV, under 80 000 V s-1 ramp rate) and b) the electron mobility (time of flight, under 40 V bias). The inset shows the bias dependence of the transit time. The slope of the data above 15 V was used to determine the mobility. The red lines represent in (a) the different current density levels and in (b) the least-squares fits to the data.[17] c) Applied bias dependence of the transit time for J_{sc} transient decay, *d* is the film thickness. The linear fit is used to calculate the limiting mobility of each film.[18] d) schematic of an FET device structure using a Si/SiO_2 or Al/Al_2O_3 gate.[19]

The CELIV method is mainly used to find out the majority carrier mobility, although it can be applied to extract the minority carrier mobility, this method is limited to certain device structures. Photocurrent transient method was applied to probe the mobility of the minority charge carrier,[18,20] by measuring the transit time (the time for photocurrent to decay to 1/e of its maximum value) over a range of applied biases, the mobility can be extract from the slope of the curve (**Figure 1.1 c**)[18]. The $PbCl_2$ treated PbS QDs film exhibited a mobility of 1.9×10^{-3} cm^{2}V$^-$

$^{1}s^{-1}$. They also came to a conclusion that the differences in mobility among the different samples are attributed to differences in electronic structure resulting from the different surface passivation but not the inter-particle spacing.[18]

As aforementioned, the TOF method requires thick film to ensure accurate measurement. In order to get the thick films, a layer by layer deposition method is usually employed, which can add artificial defects and poor performance to devices. Another technique for majority carrier mobility measurement is the field-effect transistor (FET) architecture (**Figure 1.1 d**), this method is not critical for thick films.[14] FET studies of QDs films typically use thick, low-permittivity dielectrics as the gate oxide, such as $SiO_{2.}$[19] However, the defects can form in the gate dielectric during QDs film fabrication, which can cause current leakage between the source and the drain electrodes in the subthreshold region.[14] The carrier mobility is calculated based on the source drain current (I_d)- gate voltage (V_g) characteristic, the current leakage will affect the measured carrier mobility.[14] Researchers constructed QD field-effect transistor based on a double-layer gate dielectric made of Al/Al_2O_3, they were able to build the thinnest possible gate oxide that still permits a sufficiently low gate leakage, which effectively reduces the effect of charges in the gate.[14,19] Thus, the carrier mobility measurement is more accurate.

Closer packing, bifunctional ligand approaches, and closer inter-particle distances are considered key strategies to improve carrier mobilities in QDs films.[19,21] It has been shown that charge carrier mobility is highly dependent on the coupling.[22] Recently, QDs carrier mobility was much improved by the development of surface passivation. Especially by the introducing of atomic ligand passivation, the carrier mobility of bromide ligand films approaches to 10^{-1} $cm^2V^{-1}s^{-1}$.[23] A report based on PbS nanocrystal FETs has the carrier mobility of 10^2 $cm^2V^{-1}s^{-1}$, however, the solar cell efficiency was limited.[24] Other optoelectronic parameters, such as trap density, might be of more importance to the device performance.[14]

Before the discussion of the trap density of QDs, we will first discuss about the carrier recombination (**Figure 1.2 a-d**). There are three main types of recombination in semiconductor materials and device: non-radiative recombination at defects, radiative recombination and non-radiative Auger recombination.[15] For high-efficiency devices, the properties of the active materials should be tuned to favor either radiative recombination or carrier extraction, but in all cases, the undesired non-radiative recombination losses must be minimized.[15] The defects in the band gap can act as the recombination centers, called electronic traps.[15] Free charge carriers can be trapped in these traps, and once a carrier of the opposite charge arrives at the same trap, they recombine non-radiatively (**Figure 1.2 a**), thus to reduce charge carrier populations.[14,15] Such defects can also reduce the quasi-Fermi level splitting range under illumination and lead to lower open-circuit voltage.[14] Therefore, reducing these trap states is of importance to increase QDs optoelectronic device performance.

Figure 1.2 a-d) Carriers recombination mechanisms. Illustrations showing the mechanisms for the recombination of electrons and holes; the mechanism depends on the interplay between the exciton binding energy and the charge carrier mobility.[15] e) The photovoltage transient method. Effect of a light pulse ($\Delta I_0(t)$) (i) on the measured change in V_{OC} (ii) and I_{SC} (iii) over time. The injected charge ΔQ is determined by integrating the current transient. The capacitance (iv) is obtained by dividing ΔQ by ΔV. The DOS can be calculated by integrating the capacitance over the voltage as shown, where n is the carrier concentration at each V_{OC}, A is the device area, e is the electron charge and d is the film thickness.[25] f) Density of trap states in QDs films made using solution-phase halide treated quantum dots compared with untreated quantum dots.[26] g) Defect state densities of the QDs film with different halides after solid-state ligand exchange, derived from open-circuit voltage transient decay measurement.[27] h)DOS in the bandgap calculated from transient photovoltage measurements for organic (red), inorganic (green) and hybrid (blue) passivation of PbS QDs films.[25]

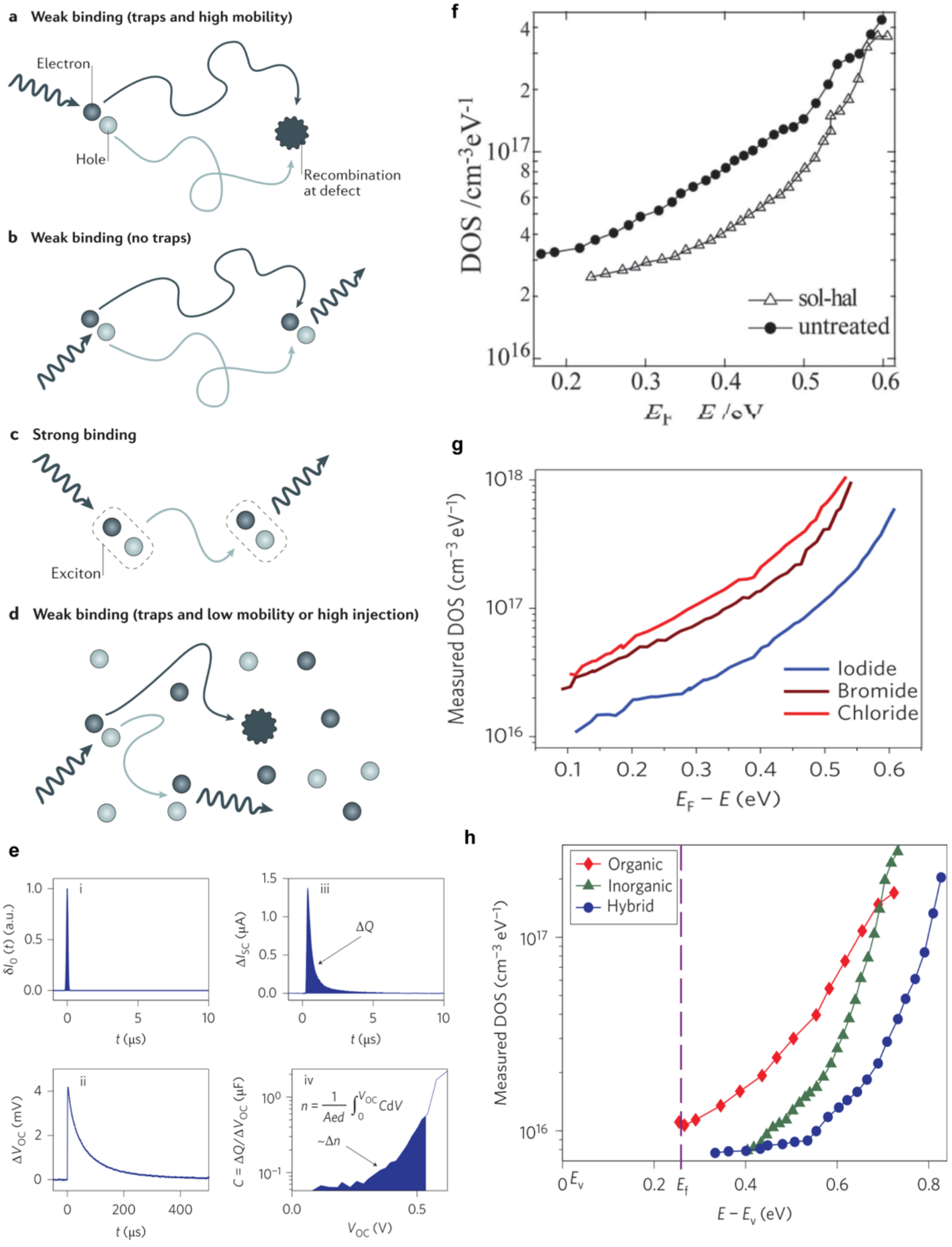
a Weak binding (traps and high mobility)
Electron
Hole
Recombination at defect
b Weak binding (no traps)
c Strong binding
Exciton
d Weak binding (traps and low mobility or high injection)
e
i
δI0 (t) (a.u.)
t (μs)
iii
ΔISC (μA)
ΔQ
t (μs)
ii
ΔVOC (mV)
t (μs)
iv
C = ΔQ/ΔVOC (μF)
n = 1/Aed ∫0^VOC CdV
~Δn
VOC (V)
f
DOS /cm-3eV-1
sol-hal
untreated
EF   E /eV
g
Measured DOS (cm-3 eV-1)
Iodide
Bromide
Chloride
EF − E (eV)
h
Measured DOS (cm-3 eV-1)
Organic
Inorganic
Hybrid
0 Ev
0.2 Ef
0.4
0.6
0.8
E − Ev (eV)

A photovoltage transient method was used to obtain the trap states density in the QDs band gap.[25] This technique is on the basis that the photogenerated charge carriers fill the mid-gap levels instead of establishing two distinct quasi-Fermi levels when illuminating a semiconductor with trap states in the band gap, thus producing a smaller open circuit voltage (V_{oc}) than of a trap free semiconductor under the same photogeneration rate[25] (**Figure 1.2 e**). Other than photovoltage transient method, deep-level transient spectroscopy (DLTS), thermal admittance spectroscopy (TAS), and Fourier transform photocurrent spectroscopy (FTPS) have been used to measure the defects in band gap.[14,28,29] The trap density can also be extracted from FET measurements by analyzing the current in the subthreshold regime.[19] Photoelectron spectroscopy (PES) can be used to characterize the trap density near the valence band edge, while inverse photoelectron spectroscopy (IPES) can evaluate the trap density near the conduction band edge.[14,18]

Such defects are normally caused by incomplete surface passivation, especially for the difficult-to-access sites. In order to reduce the undesired trap states, different surface passivation approaches have been studied. It is proved that solution-phase halide passivation leads to a lower defect concentration compared to untreated quantum dots (**Figure 1.2 f**).[26] Different halides passivation have been carried out, as **Figure1.2 g** shows that a strong ligand bonding strength on QDs surfaces is essential for band gap defect prevention.[14,27] The iodide makes the QDs films less trap states in band gap, compared with bromide and chloride.[27] Moreover, the use of hybrid ligand exchange reduces the trap density more compared with that of both pure organic and pure inorganic ligands passivation.[14] The mid-gap trap state density inside the hybrid passivated film is 2×10^{16} cm^{-3}eV^{-1}, five times lower than in conventional organic or inorganic passivated only films, **Figure 1.2 h** shows the results.[25]

Charge carrier diffusion length is the predominant parameter to the optoelectronic device's performance, since the charge carriers transport solely relies on diffusion in the diffusion region of photovoltaics. Carrier diffusion length is affected by the carrier lifetime and minority carrier mobility, lifetime is another crucial factor in device performance.[14]

Electrons and holes are generated by absorbing incident photons in semiconductor, and the density of photogenerated electrons and holes will decay with time when the illumination is off. This process of decay is recombination, where an electron and a hole recombine and annihilate each other, this time constant of decay is recombination time or carrier lifetime. The recombination-limited lifetime measurement can be achieved by open circuit voltage decay with illumination off and on.[30,31] They are using a 975 nm diode laser at room temperature, and the laser turn-off time is 3μs, the transient responses were recorded by an oscilloscope with 1 MΩ input impedance.[32] **Figure 1.3 a** shows a typical V_{oc} decay curve at an illumination of 16 mWcm^{-2}, the lifetime can be calculated with the slope of the decay curve.[32] Since the electron and hole diffuse due to concentration gradients and drift under the internal electric field, the carrier diffusion length can be calculated by combining carrier mobility and carrier lifetime.[32]

New experimental method to investigate charge carrier diffusion directly in coupled QDs solids under charge-neutral, for instance undepleted conditions.[33] This is a direct measuring method of diffusion length (L_D) experimentally in QDs materials, it is designed on light-absorbing film, removing all contact and interface effects.[33] It is the first method to take advantage of the QDs bandgap tunability and observation of the direct photoluminescence (PL) signal from the QDs to measure directly the action of diffusing carriers,[33] as **Figure 1.3 b** shows.

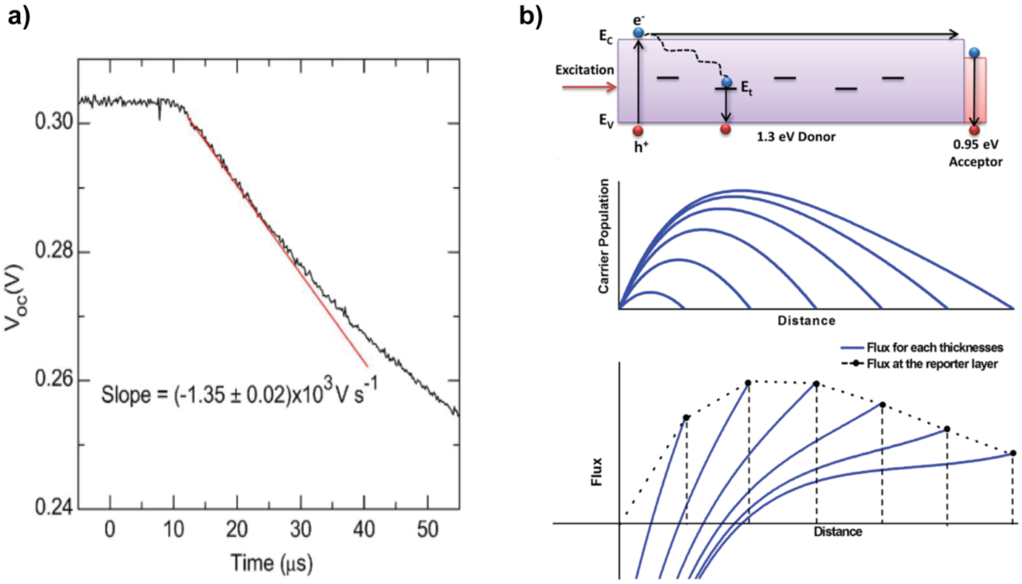

Figure 1.3 a) Representative *V_{OC}* decay signal after 975 nm, 16 mWcm^{-2} illumination turn off, a linear fit used to determine the recombination-limited lifetime. b) Schematic figure of the 1D diffusion method, a donor layer is illuminated on one end, generating a charge carrier profile within the material, carrier populations and flux obtained for several simulated film thicknesses employing in 1D model.

These diffusion length and carrier lifetime measurement methods provide us intuitional way to study the carrier diffusion mechanism, thus it provides possibility to further improve the carrier diffusion length in QDs films. Hybrid passivation technique led to improved diffusion length in QDs, was about 70 nm.[25] And the highest reported diffusion length of QDs is around 230 nm, by utilizing the combination of chemical passivation with partial fusing of certain surfaces presented by adjacent quantum dots.[34] The combination of excellent transport and reduced trap states led to the longest reported diffusion lengths observed in a colloidal quantum dot solid.[34]

As mentioned before, in the quasi-charge-neutral region outside of the depletion region, minority carriers motion relies on diffusion[35]. The common diffusion length observed to be in the range of 10-200 nm.[36] So far, Schottky devices with an opaque back contact fail to scale the active layer thickness up to beyond 200 nm, this is limited by the short diffusion length of QDs. Beyond this threshold, absorption increases but the charge generation occurs too far from the junction to achieve efficient carrier extraction, and thus the internal quantum efficiency declines.[35] In order to increase the solar cell efficiency and overcome this limitation, some good progresses have been achieved in two directions. One way is to increase the diffusion length of QDs by surface chemistry modification and the other is to improve the device architectures, such as plasmonic nanostructures and structured electrodes for light trapping.

1.1.2 QDs Optoelectronic Devices

Due to QDs unique optical properties and low-cost fabrication, QDs are widely used in optoelectronic devices, such as photovoltaics and photodetectors. Photovoltaic devices which convert solar radiation into electric power are increasingly required to offer simultaneous combination of low cost fabrication and high power conversion efficiency.[2] QDs are solution synthesized and solution processed semiconductors, which makes the fabrication cost lower than conventional Si devices. The size tunable bandgap also offers an opportunity to achieve high device performance. QDs offer an avenue to tandem and multi-junction solar cells that make excellent use of the dispersion of solar fluence as a function of photon energy.[2,37,38] They also show promise in multiple exciton generation[39] as well as photon up- and downconversion,[40] technologies that, like the multi-junction strategy, offer a roadmap beyond the Shockley-Queisser limit.[2,37]

In early research in QDs solar cells, a Schottky structure was mainly employed, wherein a layer of p-type QDs was sandwiched between a transparent conductive oxide and a shallow-work-function metal.[32,41,42] In 2010 a depleted-heterojunction architecture was developed to address the limitations of Schottky structure. Despite rapid progress in the depleted heterojunction structure, the photovoltaic performance of QDs solar cells nevertheless remains limited by a compromise between light absorption and charge extraction, limited by the short diffusion length of QDs as mentioned in previous chapter. The novel structure studied in this dissertation would pave the way to overcome this compromise as following chapters discussed.

Photodetector is another type of device would benefit from QDs' optical properties. They are converting the incident light into electrical signals, are widely used in digital imaging, optical communications, remote sensing, night-time surveillance, medical imaging and so on.[43–46] QDs based photodetector devices can be classified into three categories based on device geometries, which are photoconductors, phototransistors and photodiodes. The device architecture and configuration of a typical device based on each class is shown schematically in **Figure 1.4**.[47] Researches focusing on QDs-based photodetector devices have been well developed in this decade.[48–54]

In order to analyze, quantify and compare the performance of photodetectors, a set of figures of merit has been formulated.[55,56] The parameters of major importance are responsivity (R), signal-to-noise ratio (SNR), noise equivalent power (NEP), normalized detectivity (D*) and quantum efficiency (EQE).

The responsivity R reflects the gain of the detector and is defined as the output signal (typically voltage or current) of the detector produced in response to a given incident radiant power input. It is the ratio of photocurrent to the optical power impinging on the detector and measured in the unit of AW^{-1}.[48] The equation express for responsivity is given by

$$R = \frac{\eta q \lambda}{hc} = \frac{1}{\sqrt{1+\omega^2\tau^2}} G \qquad \text{Equation 1.2}$$

Where q is the electron charge, h is the Planck's constant, c is the speed of light, ω is the electrical modulation frequency, η is the quantum efficiency, τ is the time constant, and G is the photoconductive gain.

Noise is another important parameter to estimate the sensitivity of a photodetector, since the minimum radiant flux that can be measured by different photodetectors with the same responsivity is inversely proportional to the level of total intrinsic noise in the detector. There are four major sources of noise in photodetectors: Johnson noise, shot noise, generation-recombination (G-R) noise, and 1/f noise.[48] By taking together the responsivity and the noise performance of the detector, one can quantify the ultimate figure of merit of sensitivity.[48] The signal current produced by the input power must be above the noise level in order to be detected. The signal-to-noise ratio (SNR) is given by

$$SNR = \frac{RP}{i_n} \qquad \text{Equation 1.3}$$

Where R is responsivity, P is the incident optical power, and i_n is the noise current. The minimum optical power a detector can detect is when the SNR is equal to zero. It is called noise equivalent power, which is defined as the radiant power incident on the detector that produces a signal equal to the root mean square detector noise. By this definition, NEP takes into account both gain and noise parameters of the detector and can be related to the detector responsivity, is given by

$$NEP = \frac{i_n}{R} \qquad \text{Equation 1.4}$$

The disadvantage of using NEP to describe detector performance is that it is specific to detectors having a particular surface area.[48] The normalized detectivity or specific detectivity

($D*$), is defined as the inverse value of NEP and taking into account the detector active area, A_d, and the electrical bandwidth, B. This parameter allows for comparison among detectors of different geometries, thus enabling the evaluation of sensitivity of photodetectors.[48] The expression of $D*$ is given by

$$D^* = \frac{\sqrt{A_d B}}{NEP} = \frac{\sqrt{A_d B} R}{i_n} \qquad \text{Equation 1.5}$$

The units of $D*$ are cmHz$^{1/2}$W^{-1} or Jones. It can be interpreted as the SNR produced by a detector of 1 cm^2 surface when 1 W of optical power impinges to detector, measured with electrical bandwidth of 1 Hz. $D*$ is a function of many parameters: applied bias, temperature, modulation frequency, and wavelength.[48]

The quantum efficiency is defined as the efficiency of an incident photon results in the excitation of an electron. It is a normalized value and is equal to the number of electrons excited divided by the number of photons illuminated on the detector's active area.[48] Usually reflectance, absorbance and scattering should be taken into account, and it also called as external quantum efficiency (EQE).

As mentioned before, photodetector is categorized into three types based on device geometry, which are photoconductor, phototransistor, and photodiode. Photoconductor devices work on the principle of measuring a temporary change in resistivity (or conductivity) of the semiconductor on irradiation with light.[47] A photoconductor typically consists of a semiconducting material, single-crystalline, polycrystalline or amorphous, and two ohmic metal contacts to form a two-port electrical device (**Figure 1.4 a**).[48] Upon illumination, the conductivity changes due to a change in mobility or carrier density or both.[48,57] The conductivity increase mainly due to the photogenerated electron-hole pairs, resulting in a charge carrier density increase.[48]

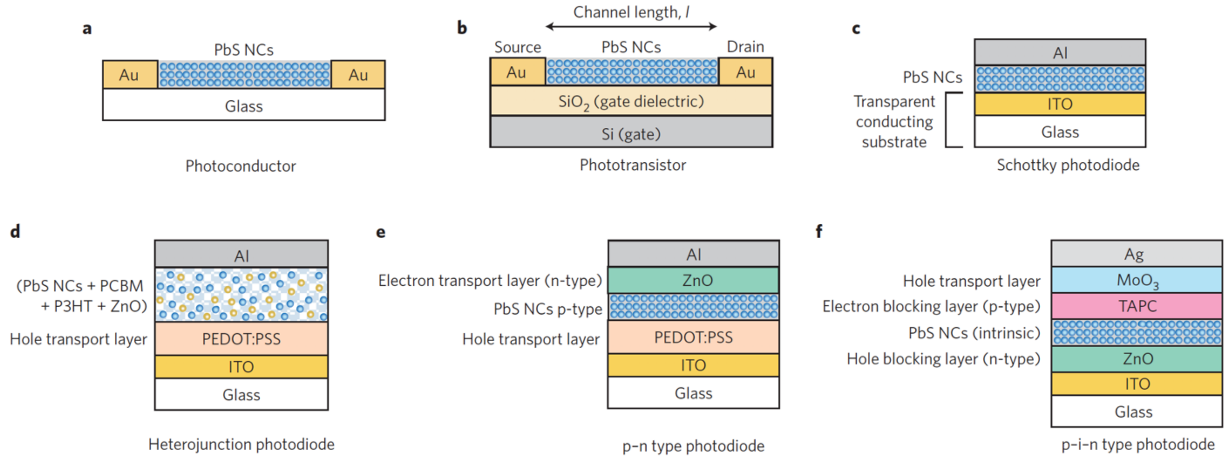

Figure 1.4 Schematic device architecture and configuration of PbS QDs photodetectors. a) Schematic image describing a simple photoconductor device architecture. b) A bottom gate phototransistor device. c) A Schottky-type photodiode configuration. d) A bulk heterojunction blended film photodiode. e) A p-n junction photodiode device. f) A vertically stacked p-i-n photodiode device.[47]

Photoconductors can offer photoconductive gain, which is greater than unity. Photoconductive gain is the ability to provide multiple electrical carriers per single incident photon,[58] is also an important property of a photodetector. The physical mechanism underlying photoconductive gain has been well studied so far. The trap states that contribute to photosensitization, also called sensitizing centers, favor to capture one carrier (e.g., electrons) over the other (e.g., holes).[48] Upon illumination, electron and hole pairs are generated, electrons are captured by these traps, whereas holes remain free to transfer in the device under the external electric field. The low capture possibility for holes prolongs their carrier lifetime. The holes, upon reaching one contact, can be replenished by the other contact.[48] The number of passes of a hole across the device is then equal to the ratio of the carrier lifetime to its transit time, giving rise to photoconductive gain G, is given by[48]

$$\tau_{tt} = \frac{1}{\mu F} = \frac{l^2}{\mu V} \qquad \left(F = \frac{V}{l}\right) \qquad \text{Equation 1.6}$$

$$G = \frac{\tau_{lt}}{\tau_{tt}} = \frac{\tau_{lt}\mu V}{l^2} \qquad \text{Equation 1.7}$$

where τ_{tt} is the transit time of the majority charge carrier, τ_{lt} is the life time of the minority charge carrier, μ is the mobility of the majority charge carrier, l is the distance between two electrodes, V is the voltage bias. The mechanism of the optoelectronic characteristics has been thoroughly studied.[57,59–61]

Phototransistor devices consist three electronic contacts, source, drain and gate electrode, as shown in **Figure 1.4 b**. This three-electrode configuration gives a greater degree of control over the conductivity of the semiconductor, owing to the ability to various gate voltage in addition to the source-to-drain voltage and the illumination intensity.[47] The negative gate voltage applied, for instance, will induce opposite charge carriers (holes) in a p-type PbS QDs film and will increase the conductivity correspondingly.[47,62] Thus, the gate electrode can be used as a switch or an amplifier, and also can control the Fermi level position. As the gain is directly proportional to the mobility of the charge carrier, hybrid phototransistors are usually fabricated by integrating PbS QDs with materials having exceptionally high carrier mobilities, for example 2D materials such as graphene,[58,63–65] and molybdenum disulfide (MoS_2).[66]

Photodiodes are based on the formation of a semiconductor and a rectifying metal contact (Schottky junction type), a junction between two different semiconductors (heterojunction type), or a semiconductor with opposite doping levels (homojunction, p-n type), and a p-i-n type (**Figure 1.4 c-f**).[47] The principle is separation of photogenerated electron-hole pairs by the action of the built-in electric field in the junction and transport of the carriers to the respective contacts for extraction.[48] Usually the charge carriers need to cross a number of device regions in order to be collected, therefore the thickness is critical and the lifetime of the carriers must be longer than the transit time.[47] Thus, the long diffusion length is desired and is critical for high quantum efficiency of the device. In PbS QDs optoelectronic devices, the diffusion length of charge carriers is not governed by their mobility alone, as well as the average spacing among the recombination centers.[67] Photodiodes can be operated at zero bias (photovoltaic mode) but are usually used under reverse bias conditions (photoconductive mode) offering high bandwidth and wide linear dynamic range.[47]

The photodetector discussed in this dissertation are mainly photoconductor and phototransistor, taking advantage of the gain effect and back gate modulation.

1.2 Current Limitations & Our Solutions

1.2.1 Limitations

As discussed in 1.1.1, the diffusion length of PbS quantum dots are usually 20-200 nm, which limits the practical thickness of QDs film to ~ 300 nm, beyond this threshold, light absorption would increase but the photogenerated electron and hole pairs occur too far from the junction to be collected, and thus the quantum efficiency would decrease. However, in order to achieve sufficient absorption of incident photons, about 1 μm of QDs films is required[35,68,69]. This is a famous compromise between light absorption and charge extraction in QDs film. With respect to achieve high device performance, thick QDs films (~ 1 μm) with efficient charge extraction is demanded.

1.2.2 Current Approaches

In order to overcome the compromise between the light absorption and charge extraction, three main approaches have been carried out. One way is to increase the diffusion length of QDs film by surface passivation, where the undesired in-gap trap states can be reduced thus decreasing the electron and hole recombination possibility. Both organic, inorganic and hybrid organic-inorganic ligand treatment are studied to improve the surface passivation. Furthermore dot-to-dot mutual surface passivation can partially fused QDs to reduce the overall surface-to-volume ratio while passivating the remaining sites led to a very low density of trap states. [34]

Another way is to modify the QDs device structure to increase either the light absorption and/or the charge collections, such as plasmonic nanostructures and structured electrodes for light trapping. The most popular technique is utilizing plasmonic light management to scatter light into trapped or wave-guided modes in the absorber layer.[70–79]

The last but not least used method to improve QDs electronic properties is to combine other 2D material with QDs. QDs film has limited conductivity due to electrons hopping from dot to dot. Thus, in order to improve the conductivity of the device, 2D materials such as graphene and MoS_2 are integrated into QDs photodetectors.

Graphene is an attractive material for photonics and optoelectronics because it offers several advantages compared with other materials,[80–89] such as the behavior of Dirac Fermions, the extremely high charge carrier mobilities up to 200 000 $cm^2V^{-1}s^{-1}$, and the abroad wavelength range light absorption,[90] However, weak light absorption and the absence of a gain mechanism limited the responsivity of graphene-based photodetectors to $\sim 10^{-2}AW^{-1}$, which is much lower than PbS QDs based photodetectors.[52,91] Two groups of pioneers reported the graphene/PbS QDs hybrid photodetectors with ultrahigh gain and responsivity.[58,91] Koppens et al. reported a graphene/PbS QDs hybrid photodetector system with ultrahigh gain and responsivity. For the previous QDs photodetectors, a photogain of 10^2 to 1×10^3 has been observed,[44,52,92] however this gain is limited by the poor carrier mobility of QDs films (1to 1×10^{-3} $cm^2V^{-1}s^{-1}$).[58] As mentioned before, graphene has extremely high carrier mobility, however it is lacking the photoconductive gain mechanism. They integrated the graphene and QDs to take advantages of the strong light absorption from PbS QDs and high charge carrier mobility from graphene. The operation mechanism of this photodetector is that photons are absorbed in PbS QDs layer and the photogenerated charges can be transferred to graphene, meanwhile the opposite charges are trapped in PbS. These trapped minority charge carriers lead to a photoconductive gain effect, the majority charge carriers induced to graphene lead to graphene conductivity change. The main feature for this device is its ultrahigh gain, which originates from the high carrier mobility of the graphene sheet (~ 1000 $cm^2V^{-1}s^{-1}$) and the recirculation of charge carriers during the lifetime of the opposite carriers that remain trapped in the PbS quantum dots.[58]

Graphene/QDs hybrid photodetectors achieved better performance than sole graphene or QDs only based devices, in terms of quantum efficiency, responsivity and speed. This paves the way towards a generation of flexible highly performing hybrid two-dimensional (2D)/zero-dimensional (0D) optoelectronics.[93] Other promising candidates for the 2D/0D optoelectronics are the atomically thin transition metal dichalcogenides (TMDCs), which also offer the opportunity to overcome the mobility-bottleneck since they demonstrate very high in-plane carrier mobility and their atomic thickness may give rise to low dark currents.[94,95] In addition, the class of TMDCs possesses large bandgap in the range of 1-2 eV, giving it a certain advantage over graphene for very sensitive photodetection: the transistor channel can be turned off by an appropriate back-gate voltage, leading to high signal-to-noise ratio.[94–97]

1.2.3 Our Solutions and Objectives

The hybrid 2D/QDs structure increases the charge carrier mobility, but the diffusion length (L_D) still stops the QDs thickness from fully absorbing light throughout solar spectrum. Herein, we demonstrate a novel photodetection architecture based on multiple intercalated graphene layers with interspacing <L_D that serve as efficient current collectors, overcoming the limitation that L_D imposes on the thickness of QD layers for charge collection. More details about the mechanism and fabrication would be discussed in the following chapter.

The goals of the current research are to develop new approach for quantum dot film to achieve desire thickness for sufficient light absorption with high quantum efficiency throughout the absorption band. In summary, the following are the objectives:

- Fabricate QDs with intercalating Gr electrodes structure to enhance the charge collection beyond QDs diffusion length.
- Study of the roles of QDs and Gr playing in light absorption and charge transfer.
- Study the charge carriers transfer between Gr and QDs.
- Achieve 1μm thickness of QDs maintaining efficient charge extraction and quantum efficiency.
- Increase the light absorption after λ >650 nm with high quantum efficiency.

1.3 Outline of the Chapters to Follow

Chapter 2 will present the first intercalated Gr films in QDs structure for enhanced charge collection. Hypothesis of this structure and detailed fabrication processes are shown, charge transport between graphene and quantum dots, lifetime of charge carriers will be presented as well. Systematic investigation of the role of graphene and quantum dots playing in charge collection and light absorption will be discussed in Chapter 3. Optimized interspacing between two graphene layers of this intercalated structure are illustrated as well. Moreover, 1-micron meter thickness of QDs film is achieved, systematic analysis of this device and more comparisons with traditional hybrid Gr/QDs devices are shown in Chapter 4. Chapter 5 will conclude this dissertation by summarizing important conclusions made in this project and proposing some research topics which may be attracting by utilizing this intercalated configuration.

Chapter 2 Intercalated QDs/Gr Hybrid Structure for Enhanced Charge Extraction

2.1 Introduction

Charge collection is critical in any photodetector and photovoltaic device. Novel materials such as quantum dots (QDs) have extraordinary light absorption properties, but their poor mobility and short diffusion length limit efficient charge collection using conventional top/bottom contacts.[35,98] In this chapter, a novel architecture based on multiple intercalated CVD graphene monolayers orderly distributed inside a QDs film is studied. The intercalated graphene layers ensure that at any point in the absorbing material, photocarriers will be efficiently collected and transported. The devices with intercalated graphene layers have superior quantum efficiency over single-bottom graphene/QD devices, overcoming the known restriction that the diffusion length imposes on film thickness. QDs film with increased thickness shows efficient charge collection over the entire λ~500-1000 nm spectrum. This architecture could be applied to boost the performance of other low-cost materials with poor mobility, allowing efficient collection for films thicker than their diffusion length.

The collection of photogenerated charges is critical in any optoelectronic device for communications, imaging, or energy harvesting. Efficient charge collection is a major issue for amorphous and nano-materials due to their short diffusion length (L_D). If photocarriers have to transit distances beyond L_D to be collected, then they will recombine without producing any photocurrent. This is the well-known restriction for conventional top/bottom contact devices: the thickness of absorbing layers should not exceed the carrier diffusion length plus depletion width (L_D+W_D). A remarkable case is semiconducting quantum dots (QDs). Despite their strong light absorption, their short L_D~50-200 nm limits the film thickness for photodetectors and solar cells to t~200-300 nm, well shorter than the light penetration depth of α >500 nm for wavelength λ>700 nm radiation.[14,99–102] This leads to poor light absorption and a big drop in external quantum efficiency (EQE) for λ>700 nm in state-of-the-art PbS QD solar cells,[100–103] being the main limitation for the power conversion efficiency.

2.2 Intercalated Gr/QDs Architecture

Herein, we introduce a novel architecture based on multiple intercalated layers of chemical vapor deposition (CVD) graphene (Gr) monolayers inside a PbS-QD film that overcomes the limitation that diffusion length imposes on the thickness. Single junction[64,66,91,93,104,105] and mixed[106,107] Gr/QD hybrid devices have previously demonstrated high photoresponsivity (PR) combining QDs for light absorption and graphene for efficient charge transport. However, the charge transfer from QDs to Gr for such single-junction (bottom graphene) configuration is still limited by the short L_D of QDs. The advantage of an intercalated configuration for charge collection is illustrated in **Figure 2.1** a-c. Thin devices have efficient carrier collection in the visible range ($\alpha_{vis} < 150$ nm), but poor collection in the near-IR ($\alpha_{NIR} > 400$ nm, **Figure 2.2 a b**). Thicker films increase light absorption, but with inefficient charge collection. Our proposed intercalated graphene layers (**Figure 2.1 c**) with graphene interspacing $D_{Gr} \leq L_D$ allows thicker absorbing layers ($t > L_D$) while keeping efficient charge collection. No matter where carriers are generated, intercalated graphene layers ensure efficient carrier collection.

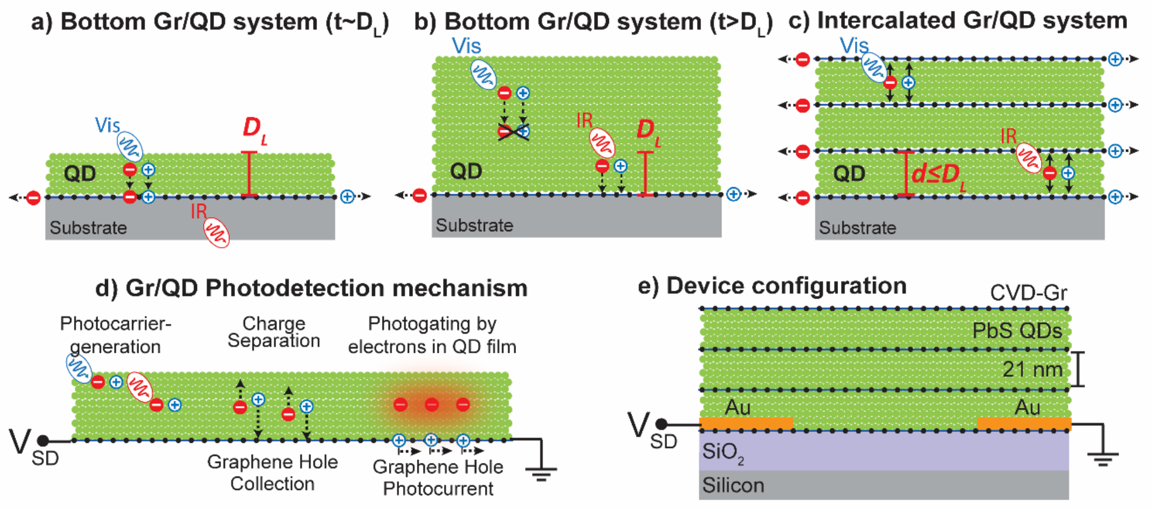

Figure 2.1 Intercalated graphene electrodes for efficient current collection. a) A thin layer with bottom configuration ensures high charge collection but has poor light absorption. b) A thicker layer enhances light absorption, but the collection efficiency is lower. c) An intercalated configuration overcomes this compromise, ensuring high absorption with efficient charge collection. d) Operation of Gr/QD photodetector junction: photo-electrons stay in the QDs film, acting as a photogate on photo-holes that are transferred to graphene and carry the photocurrent.[91,93,104] e) Device schematics, showing bottom electrodes used to apply a V_{SD} across graphene layers.

The photodetection mechanism in Gr/QD junctions is shown in **Figure 2.1 d** as reported previously:[91,93,104] under illumination, the built-in potential at the Gr/QD keeps the photo-electrons in the QDs and drives the photo-holes to graphene producing a photocurrent under a bias voltage （V_{SD}）. This behavior is also observed in our test devices. The field effect carrier mobility is ~ 1000 $cm^2V^{-1}s^{-1}$ in graphene (**Figure 2.2 c** dark line), then PbS QDs capped with tetrabutylammonium diode (TBAI) films was coated by spin coating. The Dirac point shift towards negative V_G, indicating electrons transferring from QDs to graphene and increasing of Fermi level (**Figure 2.2 c** red line). **Figure 2.2 d** shows the transfer curve of graphene with QDs transistor under different illumination power, the curves shift to higher gate voltage with increase of light illumination, indicating holes transferring from QDs to graphene under illumination and downwards of Fermi level shift.

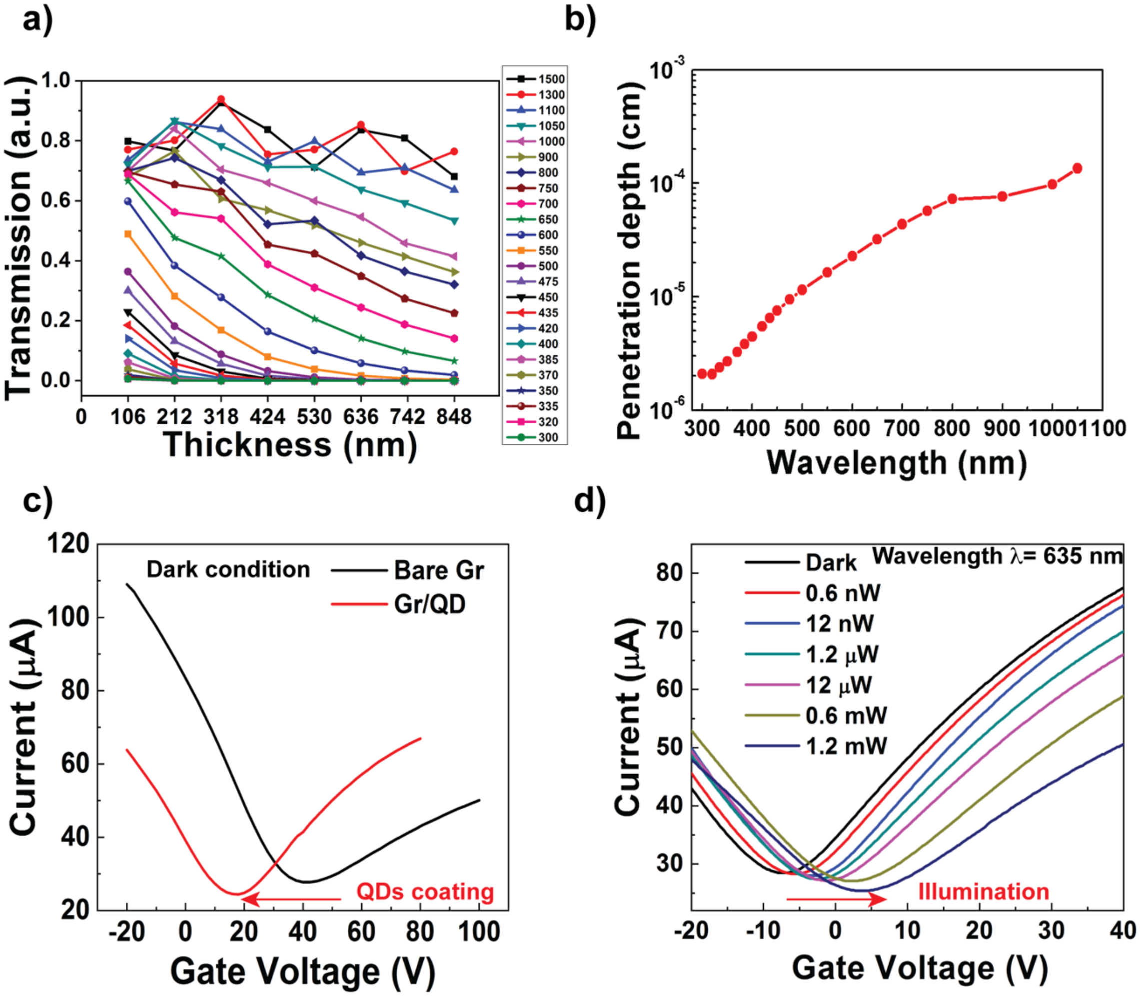

Figure 2.2 a) Transmission of 300-1500 nm light as a function of thickness for PbS QD films with emission peak at 1000 nm. Different curves correspond to different light wavelengths indicated in the right label. The thickness was estimated by multiplying 21 nm per layer by the total number of layers. The thickest film was made of 40 layers. b) From top figure, the penetration depth as a function of wavelength was extracted by fitting to the Beer-Lambert Law ($e^{-\beta/z}$). For 700 nm, the estimated penetration depth is 4×10^{-5} cm (~400 nm). c) After QDs coating, the curves shift towards negative V_g, indicating a transfer of electrons and an increase in Fermi level. The mobility of the graphene layers is μ~1000cm^{2}V^{-1}s^{-1}. d) Under illumination, the curves shift towards positive V_G indicating a transfer of holes and downwards Fermi level shift. This is due to the built-in potential formed at the Gr/QD interface that drives the photogenerated holes to graphene and keeps the electrons in the QD film, producing a photogating effect.

2.2 Intercalated QDs/Gr Architecture and Fabrication

In order to achieve the intercalated graphene in QDs structure as **Figure 2.1 e** shows, graphene transfer and PbS QDs spin coating are applied sequentially.

2.2.1 CVD Monolayer Gr Transfer and PbS QDs Film Processing

Scalable area and uniform single-layer graphene has been successfully synthesized using chemical vapor deposition (CVD) method on target substrate, such as copper and nickel.[108,109] And this monolayer graphene are able to be transferred to a various of substrates by poly (methyl methacrylate) PMMA supporting transfer. [80,110]

Figure 2.3 is the schematic images of the graphene transfer process. Monolayer graphene film used in this work were purchased from Graphenea, there is a thin layer of PMMA film on top of graphene to assist the transfer and protect graphene. The sample was placed in ammonium persulfate solution (APS) until the copper foil was dissolved, then the film was transferred to DI water bath 3 times to remove the etchant residuals, then was transferred to target Si substrate and dry overnight. The dry graphene film on substrate was immerged in acetone to dissolve PMMA, and isopropanol bath was followed.

A variety of processing methods have been developed to create stable, robust, high-quality colloidal quantum dot films.[14] The major methods used in research or small scale production are batch-driven deposition methods, spin coating, drop casting, and dip coating are the most commonly used techniques. These techniques are sufficient to form the QDs films for the study of mechanisms, characteristics and properties of QDs.

Spin coating was utilized in this work to form the QDs film, and TBAI ligand treatment was applied. As **Figure 2.4 a** shows, the substrate is held onto a rotational vacuum chuck, and after deposition of the initial solution, the stage is spun at typical speeds of 1000 - 3000 rpm, leading to spreading and shearing of the deposited solution.[14] The thickness of the final film is dependent on the spin speed and solution viscosity, a constant spin speed usually leads to reproducible and uniform thin films.

In this work, PbS QDs solution (30 mg/ml in toluene) was spin coated at 2500 rpm for 30s, then a solid-state ligand exchange was performed by flooding the surface with 0.03 M tetrabutylammonium iodide (TBAI) in methanol for 30s before final spinning dry at 2500 rpm. In thin films fabrication, layer-by-layer deposition is usually used to achieve a desired thickness,[111–113] which is conducted by repeating the film deposition several times. The progress in QDs ligand exchange enables closer packing of the quantum dots, which leads QDs to be less soluble and make it possible for the next layer to be deposited, as well as improved electronic properties.[114,115] Thus, the layer-by-layer deposition can be applied by using spin-coating to build up a film of desired thickness.

SEM image of five time repeating the film deposition of QDs film is shown in **Figure 2.4 b**, the total thickness is ~ 107 nm, indicating that each spin coated QDs layer is ~21 nm. This is also applicable to the intercalated Gr/QDs films (**Figure 2.4 c**), total five-time spin coating of QDs film is ~ 105 nm. The intercalated Gr/QDs film fabrication process would be discussed in following part.

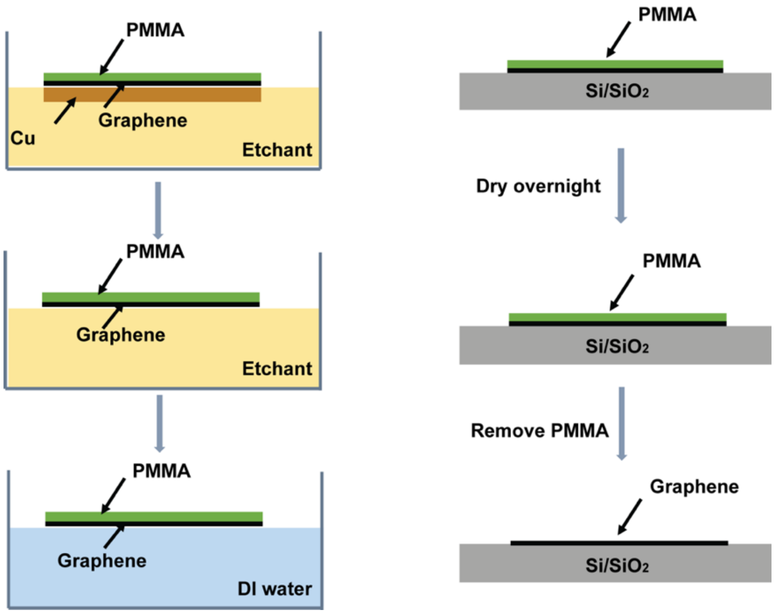

Figure 2.3 Monolayer graphene wet transfer by PMMA supporting, Cu is etched by ammonium persulfate (APS) solution, then transferred to DI water bath to remove the etchant residuals and transferred to target substrate and dry overnight, PMMA is removed by acetone bath at the last step.

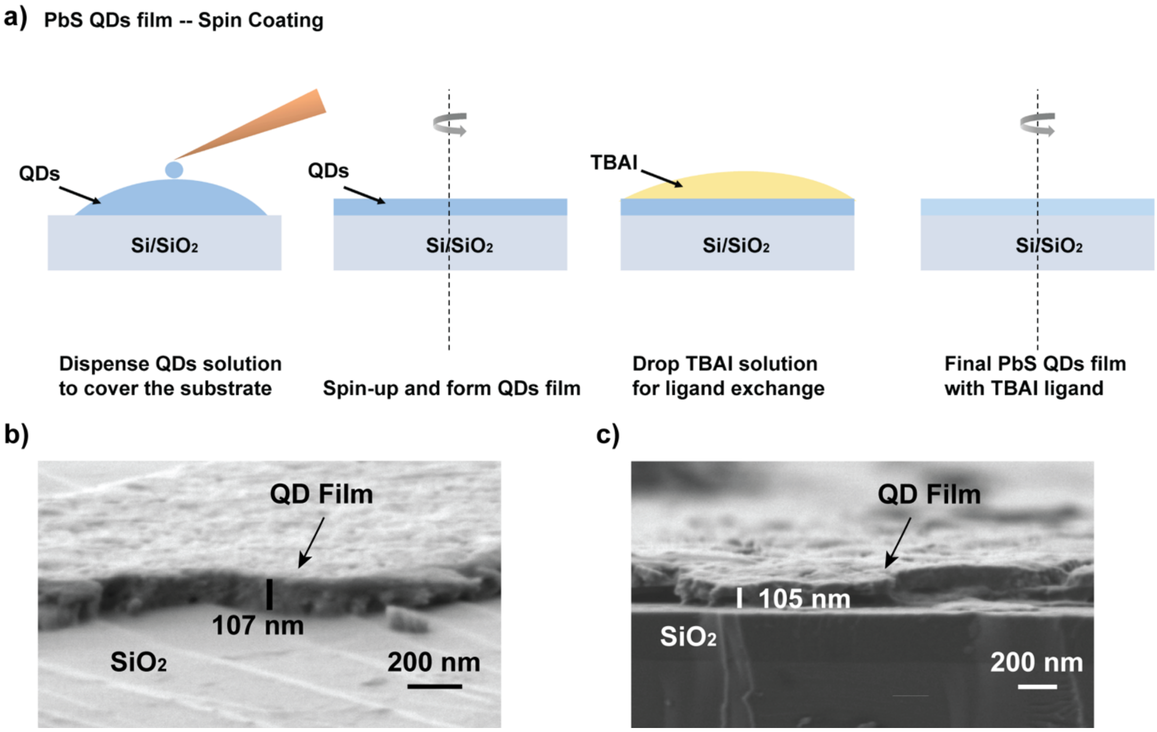

Figure 2.4 a) QDs film formation by spin coating and ligand exchange treatment.

2.2.3 Intercalated Gr/QDs Structure

By alternating utilizing the monolayer Gr wet transfer and PbS QDs film spin coating (discussed before) on SiO_2/Si chips with predefined Au/Cr electrodes (**Figure 2.5 a**). Optical images and photoresponse (AM 1.5 illumination) as Gr and QDs layers are added sequentially on the same device are shown in **Figure 2.5 a b**. The initial QD/Gr (t ~20 nm) shows a dark current of I_{off} = 62 μA and a photocurrent of $I_{ph} = I_{on} - I_{off}$ = 13 μA. After a second Gr and a third QDs layer (QD/Gr/QD/Gr/QD), I_{off} increases twofold to 170 μA due to a second graphene channel, while I_{ph} increases almost three-fold to 40 μA. This clearly indicates a conductivity and photocurrent increase when Gr and QDs layers are added. The conductivity and photoresponsivity vs. thickness of independent devices are shown in Figures 2.2 c-d. Bottom devices have a single Gr collector at the bottom, whereas intercalated devices have a Gr layer after each QDs layer. The graphene interspacing corresponds to the thickness of each QDs layer (~21 nm) and the estimated thickness is just 21 nm times the number of QDs layers, neglecting graphene thickness (Figure 2.3). The conductivity for bottom devices is constant as expected, while for intercalated devices it increases linearly due to added Gr conductive channels. Figure 2.3 d shows that for bottom devices the photocurrent slightly increases from t = 20 to 100 nm but then decreases from t = 140 to 200 nm due to lower charge collection. In contrast, intercalated devices show a stronger and steady increase in photocurrent, overcoming the limit that L_D imposed on charge collection on bottom devices.

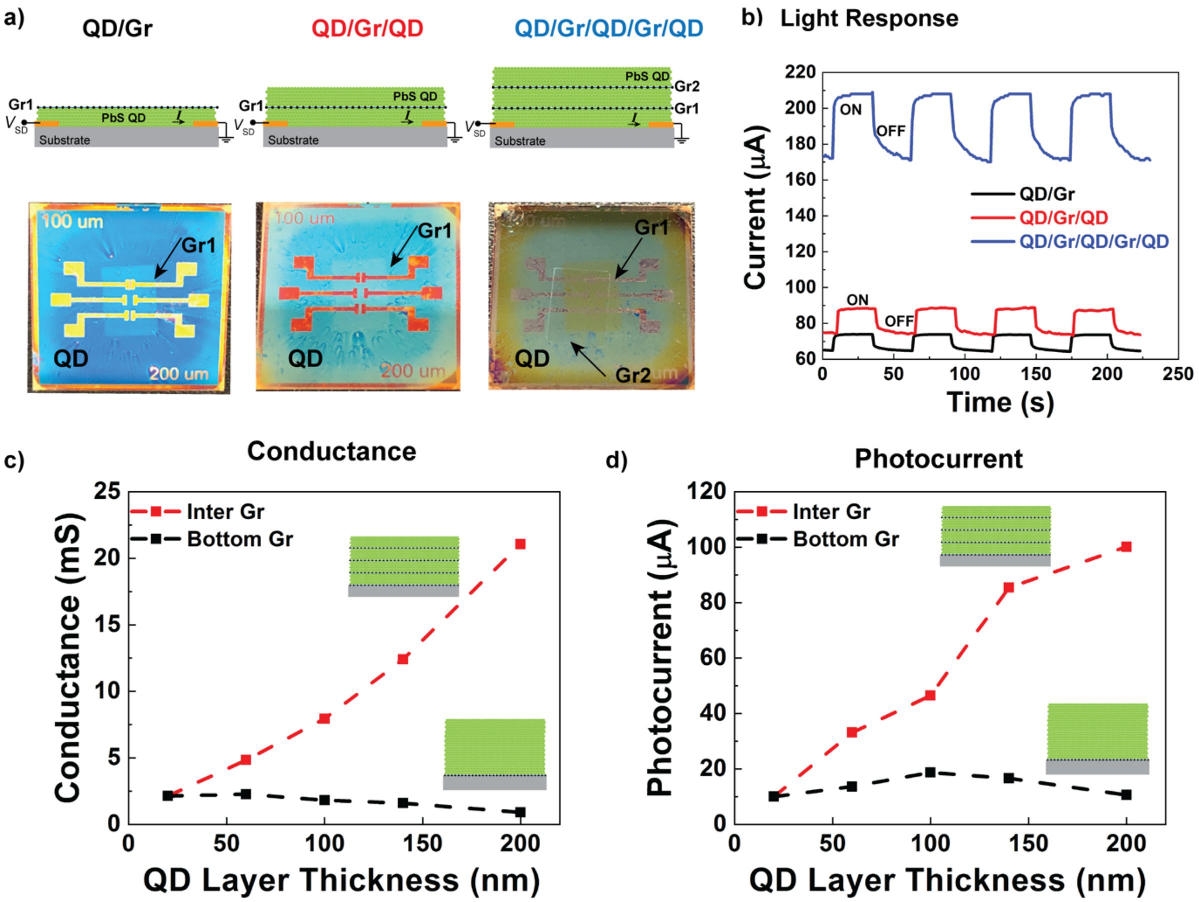

Figure 2.5 Conductivity and photocurrent evolution. a) Optical images and b) light response evolution for as Gr and QD layers are added on the same chip showing the increase in conductivity and photoresponsivity under 40 mV bias. The estimated thickness of each QD layer is 21 nm. c) Conductance and d) photocurrent as a function of thickness for bottom (non-intercalated) and intercalated Gr/QD devices. Intercalated devices show a steady increase for both. Bottom devices have constant conductivity, while their photocurrent increases from 20 to 100 nm followed by a decrease from 140 to 200 nm. Illumination: AM 1.5 solar simulator.

2.3 Spectral Response of Intercalated Device and Bottom Device

The spectral photoresponse ($PR = I_{ph}/P_{inc}$) of bottom devices shows that in the λ~500–700 nm range, the thinnest device (t = 20 nm) has the strongest response (**Figure 2.6 a**). However, for λ > 800 nm thicker t =100 nm and 200 nm devices have higher responses. This shows the trade-off for the bottom configuration: thin layers efficiently absorb and collect charges in the visible, while thicker layers fail to collect carriers in the visible but show higher response at λ >800 nm due to its deeper absorption. **Figure 2.6 b** shows that this compromise is overcome using intercalated collectors. The t = 100 nm and t = 200 nm thick intercalated devices have higher *PR* than bottom devices with same thickness across the entire λ = 500-1100 nm range. For t = 200 nm, the intercalated device has a *PR* 4× higher than the bottom device. This shows that light absorption is increased while keeping efficient charge collection for all wavelengths. Consequently, the quantum efficiency of intercalated devices shows a steady increase as the thickness increases (**Figure 2. 6 c**). The quantum efficiency is given by:

$$EQE = PR \times \left(\frac{hc}{q\lambda}\right) \qquad \text{Equation 2.1}$$

For bottom devices, *EQE* decreases as thickness increases for λ ~630 nm but increases marginally for λ ~1000nm (**Figure 2.6 d**). In contrast, *EQE* of intercalated device has a strong enhancement for both λ ~630 nm and λ ~1000nm, clearly breaking the compromise between thickness and charge collection.

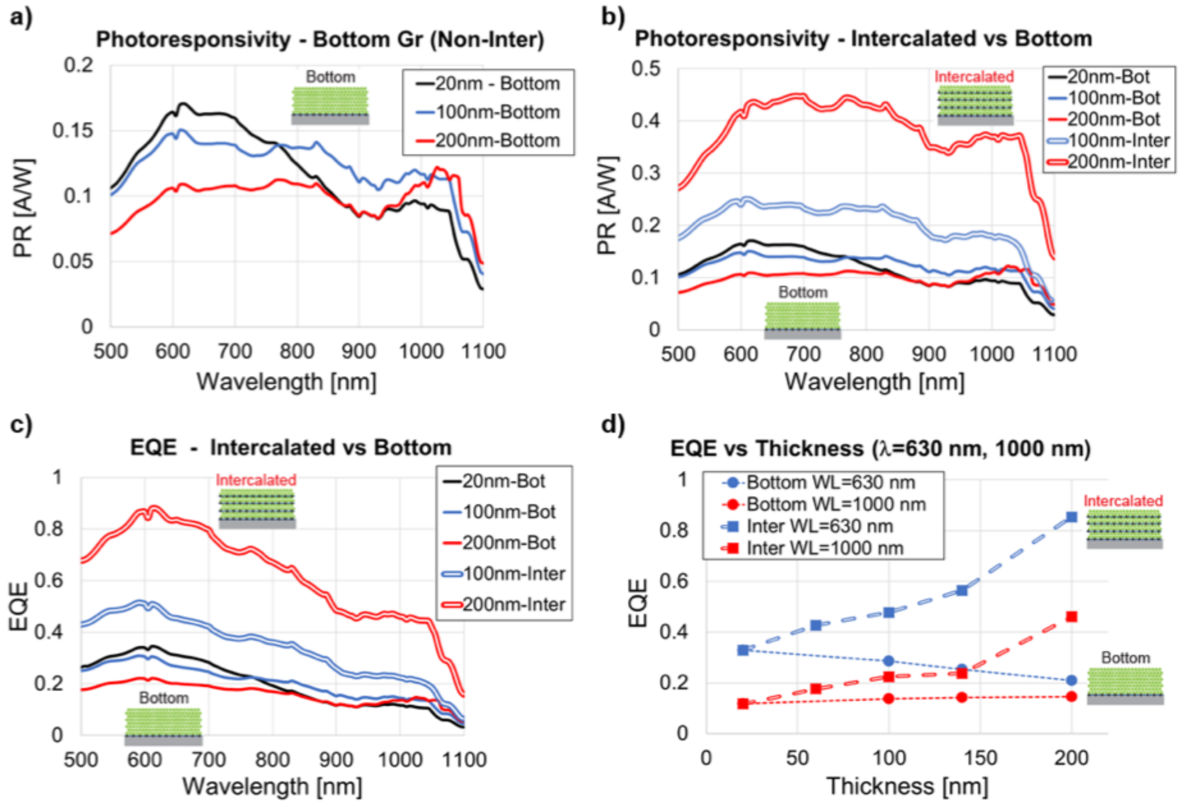

Figure 2.6 Spectral response. a) Photoresponse ($PR = I_{ph}/P_{inc}$) for bottom devices, under 40 mV bias. For $\lambda < 800$ nm, the thinnest 20 nm device has the highest *PR*, whereas 100-200 nm thicker devices have higher PR for $\lambda > 800$ nm. b) Intercalated devices show superior performance in the entire range from 500 to 1000 nm. Both 100 and 200 nm thick intercalated devices have higher *PR* than bottom devices with same thickness. c) *EQE* showing superior charge collection across spectrum for intercalated devices with respect to bottom devices. d) *EQE* as a function of thickness. Bottom devices show *EQE* reduction as the thickness increases for incident light with $\lambda = 630$ nm, and a marginal increase at $\lambda = 1000$ nm. Intercalated devices show higher and steady increase with thickness for both $\lambda = 630$ nm and 1000 nm. (Light intensity: ~10 $mWcm^{-2}$).

2.4 Charge Transport in Intercalated Device and Quantum Efficiency Calculation

The superior performance of intercalated devices was also observed for QDs with 1400 nm emission. As shown in **Figure 2.7 a**, intercalated devices show superior *EQE* across spectrum compared with the bottom devices. The *PR* dependence on light intensity with a $\lambda = 532$ nm laser is shown in **Figure 2.7 b**. At low power of 1×10^{-5} $mWcm^{-2}$ and for 100 nm thick devices, *PR* reaches 5.94×10^{7} AW^{-1} for the intercalated device, higher than 3.86×10^{7} AW^{-1} for the bottom device. Both devices show an increase in *PR* as the power decreases as previous reports on QD[53] and Gr/QD devices,[91,104,116] due to higher recombination rate, reduced built-in potential, and saturation of sensitizing traps in QDs as power increases.[91,104,117,118] At low power, the long lifetime of electrons ($\tau_{life\text{-}el}$) in trap states and the short transit time of holes in graphene ($\tau_{tr\text{-}h}$) produce a large photogain (*G*), is given by: [119]

$G = \tau_{life-el}/\tau_{tr-h}$ Equation 2.2

$\tau_{tr-h} = L^2/(\mu \times V_{SD})$ Equation 2.3

where *L* is the channel length, μ is the carrier mobility, V_{SD} is the voltage applied between the source and drain. The lifetimes are $\tau_{life\text{-}el}$ ~3s for intercalated and ~8.6 s for the bottom devices as extracted from time decay response (**Figure 2.7 c**), giving corresponding gains of $G = 1.5\times10^8$ and 4.3×10^8, calculations as followed.

At the low power regime, ~10^{-5} mWcm^{-2}, the photoresponse is greatly enhanced by the photogain, resulting from the longer lifetime of the electrons in the QDs over the short transit time of the holes traversing the graphene channel.[119] The *EQE* for 1400 nm was obtained by the expression

$PR = \frac{I_{ph}}{P_{inc}} = (QE)(\frac{q\lambda}{hc})G$, where $G = \frac{\tau_{lifetime}}{\tau_{transit}}$ Equation 2.4

Given the parameters of our devices with L=100 μm, V_{SD}=5 V, and μ=1000 cm^{2}V^{-1}s^{-1}, we obtained the transit times of holes in graphene:

$\tau_{tr\text{-}hole} = \frac{L^2}{\mu V_{SD}} = 20$ ns Equation 2.5

The lifetimes are extracted from **Figure 2.7 b**: Intercalated: $\tau_{life\text{-}el} = 3$ s, and Bottom: $\tau_{life\text{-}el} = 8.6$ s.

The photogain ($G = \frac{\tau_{life-el}}{\tau_{tr-hole}}$) are: Intercalated: $G = 1.5\times10^8$, and Bottom: $G = 4.3\times10^8$.

The corresponding *EQE* can be extracted from

$$EQE = \frac{PR}{G\left(\frac{q\lambda}{hc}\right)},$$

For the intercalated device with thickness $t = 100$ nm using an excitation with $\lambda = 532$ nm:

$PR = 5.94 \times 10^{7}\ \mathrm{AW^{-1}}, \rightarrow EQE = 0.90$

For the bottom device with thickness $t = 100$ nm using an excitation with $\lambda = 532$ nm:

$PR = 3.86 \times 10^{7}\ \mathrm{AW^{-1}}, \rightarrow EQE = 0.21$.

More quantum efficiency results are shown in the following table, the 1000 nm QDs were under an excitation with $\lambda = 635$ nm.

Table 2.1 Quantum efficiency and other parameters of 1000 nm and 1400 nm PbS QDs

QDs Emission Wavelength	Thickness	EQE	PR [A/W]	G	Decay Time [s]	PL Lifetime [ns]
1000 nm	100 nm	74.59 %	9.72×10^{7}	2.55×10^{8}	5.1	N/A
	200 nm	82.69 %	1.20×10^{8}	2.85×10^{8}	5.7	N/A
1400 nm	100 nm	89.55 %	5.94×10^{7}	1.55×10^{8}	3.1	9
	200 nm	93.91 %	8.44×10^{7}	1.70×10^{8}	4.2	N/A

This corresponds to *EQE* of 0.90 and 0.21 for the intercalated and bottom system, respectively. Photoluminescence lifetimes (τ_{PL}) were also measured, giving shorter lifetimes for intercalated devices, τ_{PL} ~5.8 ns, than for bottom devices, τ_{PL} ~9 ns, suggesting faster charge separation and collection for intercalated devices as well.[34,120,121] Charge transfer in bottom and intercalated systems may have different transport regimes. Bottom devices have a depleted area near graphene followed by a diffusion-regime zone. In contrast, in intercalated devices all the QDs are within ~10 nm from graphene layers, thus an entire depleted-drift regime is probable.

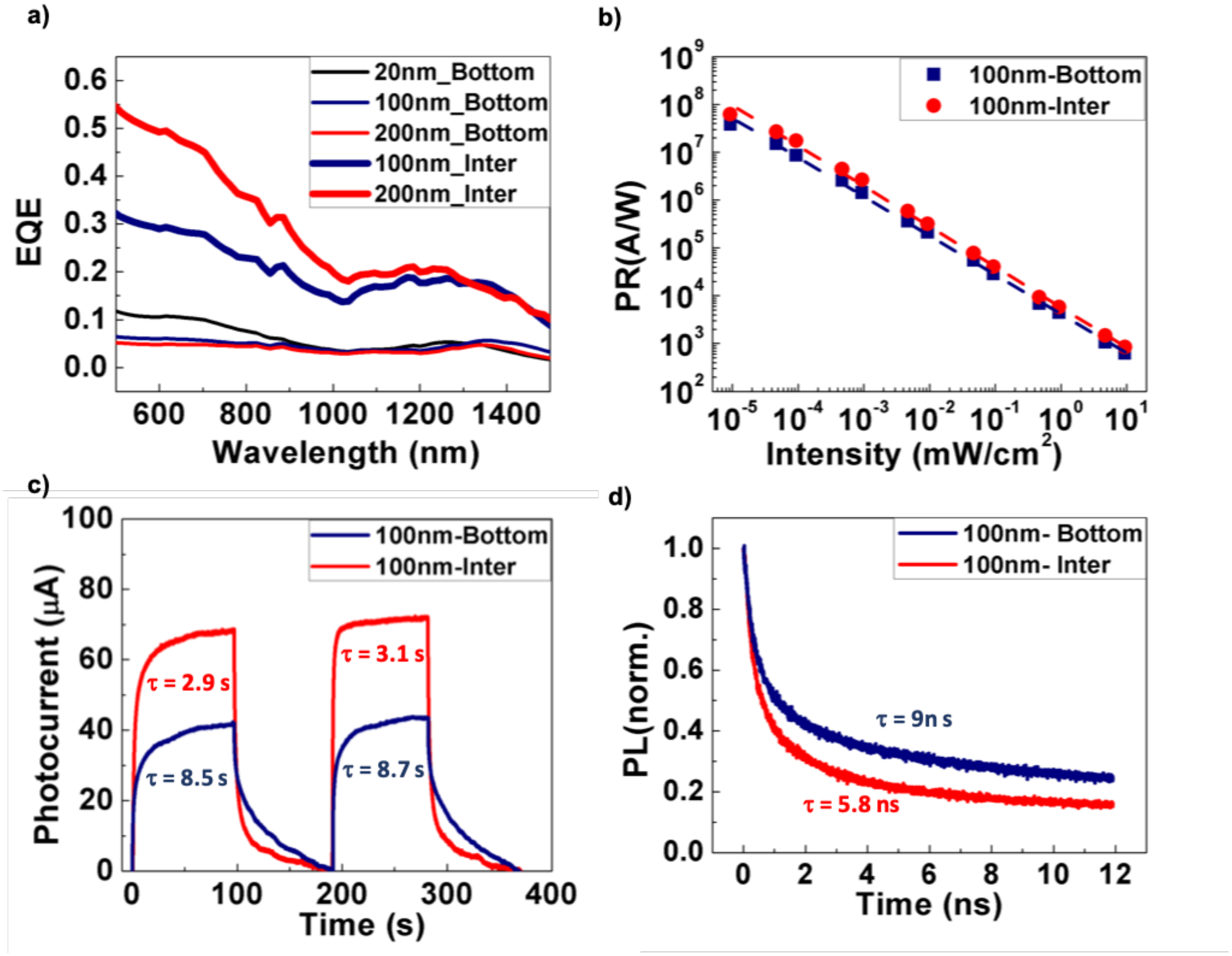

Figure 2.7 Power dependence, time response and PL lifetime. a) *EQE* of QDs with 1400 nm emission showing superior EQE for intercalated devices over bottom devices as well. b) *PR* increases as light intensity decreases, with higher *PR* for the intercalated than for bottom device. Device under V_{SD}=5 V and 532 nm laser diode. c) Time response, showing decay time of ~3 s for intercalated device and 8.6 s for bottom device. d) *PL* lifetime showing shorter decay time for intercalated (5.8 ns) than for bottom devices (9 ns).

2.5 Conclusion

Compared to previously reported single junction Gr/QD devices, our intercalated devices have higher quantum efficiencies, reflecting superior charge collection. Konstatatos et al[104] reported an *EQE* of 0.25 at λ ~532 nm for t = 80 nm bottom Gr/QD devices, which is comparable to our *EQE* of 0.21 (λ ~532 nm) for t = 100 nm bottom devices. In contrast, our t = 100 nm intercalated device achieves a higher *EQE* of 0.90. Based on the similar bottom junction performance, we presume that the *EQE* gain is mainly due to the intercalated configuration and not to material properties. However, our intercalated devices are slower and have lower photogain. Further comparisons showing superior charge collection (*EQE*) of our intercalated devices with respect to other previous works with Gr/QD devices[91,104,116] would be discussed as followed.

The work from Koppens *et al* published in Nature Nanotechnology[58], was seminal showing the capability of the hybrid Gr/QD system. They demonstrate ultrahigh gain with a hole transit time of 1 ns and electron lifetime of 1 s. They demonstrate a PR of 5×10^7 AW^{-1}. Compared to our results, their bottom-single Gr/QD junction device has higher gain and faster response. However, they report an *EQE* of 25% for an 80 nm thick QD with bottom graphene. Our intercalated device 100 nm thick achieves an *EQE* of 90%, demonstrating higher charge collection. The work from Nikitskiy *et al*[93] integrates a top gate electrode to actively control the QD/Gr photodetector. It is a versatile device that operates as both photodiode and phototransistor, with a bandwidth operation of 1 kHz, achieving much higher speeds than our intercalated device. However, in terms of charge collection, their devices reach 10% at $V_{TD} = 0$ and up to 80% at $V_{TD} = 1.5$ V with a 300 nm thick layer. Our device reaches ~90% without any gate voltage and using a much thinner 100 nm QDs layer. The work from Feng Yan *et al*,[91] was the first single CVD graphene and QD hybrid device focused on infrared detection (λ~895 nm) achieving PR~10^7 AW^{-1} and remarkably building also flexible devices. Their devices have very similar geometry and properties to our intercalated devices, namely same channel length L = 100 µm, mobility of $\mu = 1000$ $cm^2V^{-1}s^{-1}$, time-response ~1-10 seconds and V_{DS} =5 V. At power intensities of 10^{-5} $mWcm^{-2}$, they obtain a PR of 10^7 A/W with a 150 nm thick film bottom-graphene, whereas we obtain a PR of 5.9×10^7 AW^{-1} with a 100 nm thick film intercalated device.

Despite the superior performance of intercalated photodetectors, their *EQE* is still similar to state-of-the-art photovoltaic (PV) devices with top-bottom contacts.[100,101,103,122] However, such PV devices have an optimized QD/ZnO junction with a higher built-in potential and they still suffer the limitation of L_D on thickness. The intercalated devices can further be improved by optimizing the Gr/QD junction as proven for other 2D/QD system.[119,123] The film thickness in intercalated systems can also be increased, however, our current devices fail to collect photocurrent from top graphene layers beyond 200 nm thick layers. Adding contacts to each graphene layer and vertical interconnect access (VIAs) would allow optimal contacts for thicker layers and open a route to reach >500 nm thickness for more efficient absorption of λ~700-1000 nm sunlight. Moreover, beyond using graphene and PbS QDs, this layer-by-layer multi-stacking intercalated configuration can enhance the device performance by using other materials. 2D atomic sheets transition metal dichalcogenides (TMDs), such as MoS_2 could be a substitute for graphene as the intercalated charge collector. Other light absorbing materials can also be used, for instance, different types or different sizes of QDs, or amorphous Si. In particular, materials with short diffusion length would benefit most from this configuration.

In conclusion, the intercalated architecture shows an enhanced performance compared to conventional bottom contacts, producing a higher *EQE* across the spectrum as the thickness is increased. The intercalated graphene layers ensure an efficient charge collection despite the thickness increment, breaking the limitation that L_D imposes on film thickness. Further studies are required to optimize the graphene interspacing, improve charge separation at Gr/QD interface, and identify diffusion/drift regimes near the Gr/QD boundary. Furthermore, the intercalated architecture can be used not only for QDs, but in any system limited by short diffusion length and in absorbing layers for deep penetrating radiation. The presented strategy can be compatible with

QD surface passivation techniques. A combination of intercalated charge collectors and enhanced surface passivation can be the route to achieve new performance records for QD photodetectors and solar cells.

This chapter, in full, is a reprint of the material as it appears in “Improved Charge Extraction Beyond Diffusion Length by Layer-by-Layer Multistacking Intercalation of Graphene Layers inside Quantum Dots Films”. Chen, Wenjun; Castro, Joshua; Ahn, Seungbae; Xiaochen Li; Vazquez-Mena, Oscar. Advanced Materials, 31, 1-6 (2019). The dissertation author was the primary investigator and author of this paper.

Chapter 3 Implementation of Vertical Interconnect Access in Intercalated Graphene/Quantum Dot Structure

3.1 Introduction

Colloidal quantum dots (QDs) are of great interest in optoelectronic and photovoltaic devices with low-cost processing, strong light absorption, and size tunable direct band gap. However, their limited charge carrier mobility and short diffusion length limit their efficient charge collection and transport. The short diffusion length in QD solid films, 100-200 nm, limits their thickness to t ≈ 200-300 nm, which results in very poor absorption in the near-infrared zone, λ >700 nm, wasting a significant part of sunlight and reducing power conversion efficiency. Recently, a novel architecture based on multiple graphene monolayers (Gr) intercalated inside QD films was reported to improve charge extraction beyond QDs diffusion length. The intercalated graphene layers ensure that photocarriers are more efficiently collected even if the QD films are thicker than the diffusion length. However, this architecture still fails to collect carriers from the quantum dots when the thickness of the hybrid Gr/QD film thickness is >~200 nm due to the poor vertical conductivity of the devices. Herein, we present the fabrication, optimization and implementation of intercalated devices with vertical interconnecting contacts, increasing carrier collection and photocurrent in hybrid Gr/QD photodetectors, aiming to develop a novel architecture for improved photodetection and photovoltaics with QDs. First, we analyze the individual roles that Gr and QDs play in the light response of intercalated devices, studying the evolution of light absorption, photocurrent (I_{ph}), and conductivity as successive QD and Gr layers are added. We find the optimal interspacing between graphene layers in the intercalated system, aiming for the best compromise between light absorption and efficient charge transfer from the

QDs to Gr. Our main contribution is demonstrating the implementation of vertical interconnect access (VIAs) gold contacts to each graphene layer, ensuring efficient charge transfer from Gr to the gold electrical contacts for efficient current collection. The Gr/QDs intercalation with VIAs allows building QD absorbing films 400 nm thick while keeping efficient charge collection. We show that for 850 nm wavelength illumination, the photocurrent of a 400 nm thick QD intercalated device is 97.5 μA without VIAs and 1.26 mA with VIAs, meaning a ~10 fold improvement. We also use a back-gate voltage to monitor Fermi level shift in Gr and charge transfer from QDs to Gr. The intercalated configuration with VIAs contacts herein presented is a significant improvement in charge collection for QD optoelectronic applications as well as a promising architecture to enhance the power conversion efficiency for QD solar cells.

Efficient charge collection and transport is critical for optoelectronic devices. Despite its low-cost processing, strong light absorption, and size tunable direct band gap, quantum dots (QDs) have poor mobility, limiting its charge collection and its overall performance in optoelectronic devices and power conversion efficiency.[2,38,44,47,54,125] Charge carrier transport in solid films of QDs occurs from dot to dot by hopping across surface organic ligands.[126,127] In order to overcome this restriction, recently graphene has been added as efficient charge collection and transporting layer as shown in **Figure 3.1a**, resulting in significant improvements on photoresponsivity and film conductivity.[91,93,104,117] Since the charge carrier mobility of graphene (Gr) (~10^3 $cm^2V^{-1}s^{-1}$)[45,128] is far superior than for PbS QDs (~10^{-3} $cm^2V^{-1}s^{-1}$)[18,32] the carrier transport is greatly enhanced. A further enhancement was achieved by adding intercalated graphene layers instead of a single bottom graphene layer as shown in **Figure 3.1b**, adding more conducting channels and facilitating the collection of photocarriers.[129] Charge carriers in QDs can reach a nearby graphene much easier in intercalated devices than in bottom devices, improving quantum efficiency and photoresponsivity.

Herein, we analyze individually the role that Gr and QDs play both in the charge transport and in the collection of photogenerated carriers. We study the evolution of light absorption, photocurrent (I_{ph}), and conductivity in intercalated film as successive QD and Gr layers are added, allowing to pinpoint their individual role in the optoelectronic response of the devices. Furthermore, we also optimize the interspacing distance between Gr layers in intercalated devices. Large interspacing between Gr layers facilitates making thicker QD films with strong light absorption, however, this also compromises the charge collection due to the short diffusion length of carriers in QDs. We also present a significant improvement to the intercalated architecture by adding vertical interconnect access (VIAs) gold electrodes. The VIAs connect with each Gr layer, significantly improving the current collection from all graphene intercalated layers, overcoming the poor vertical conductivity through the quantum dots. The VIAs allows efficient charge collection in films thicker than 200 nm, the limit for the previous report of intercalated devices relying only on bottom gold contacts.[129] Herein we reach 400 nm thick films, achieving stronger light absorption while keeping efficient current collection. We also study the device performance as function of light power intensity. The devices show an increase in photoresponsivity as light power intensity decreases. Furthermore, despite having intercalated Gr layers, we are able to modulate the carrier density of the graphene layers through a back electrostatic gate, tuning the device photoresponse and allowing to identify the transfer of holes from QDs to Gr as the main light response mechanism. The intercalated architecture optimizing graphene interspacing and incorporating VIAs is an effective way to increase I_{ph}. This configuration can serve as a basis to potentially increase power conversion efficiency in QD solar cells through intercalated electron and hole collectors.

3.2 The Role of Gr and QDs Films in Charge Transport and Light Absorption

Intercalated layers of graphene in QDs films are realized by sequential deposition of Gr and QDs as shown in **Figure 3.1c**.[80,130] CVD Graphene monolayer grown on copper foils (Graphenea, Spain) was transferred onto SiO_2/Si chips using the common wet transfer using PMMA as polymer support. For QDs, PbS nanoparticles with bandgap of 1.2 eV (λ = 1000 nm emission) were used and deposited by spin coating with TBAI (tetrabutylammonium iodide) as surface capped ligand. Sequential transfers of graphene and spin coating of QDs allows to produce intercalated devices with varying thicknesses. In between graphene layer depositions, the spin coating of QDs can be repeated in order to have thicker QD films in between graphene layers, effectively increasing the graphene interspacing (D_{Gr}). **Figure 3.1d** shows optical images of the devices as Gr and QD layers are added during the fabrication process. Scanning electron microscopy images indicate that the thickness for each spin coated QD layer is ~20 nm (**Figure 3.1 e f**). In the intercalated Gr/QDs device, the QDs film is separated by graphene layers, well in bottom device QDs film is a continuous bulk film.

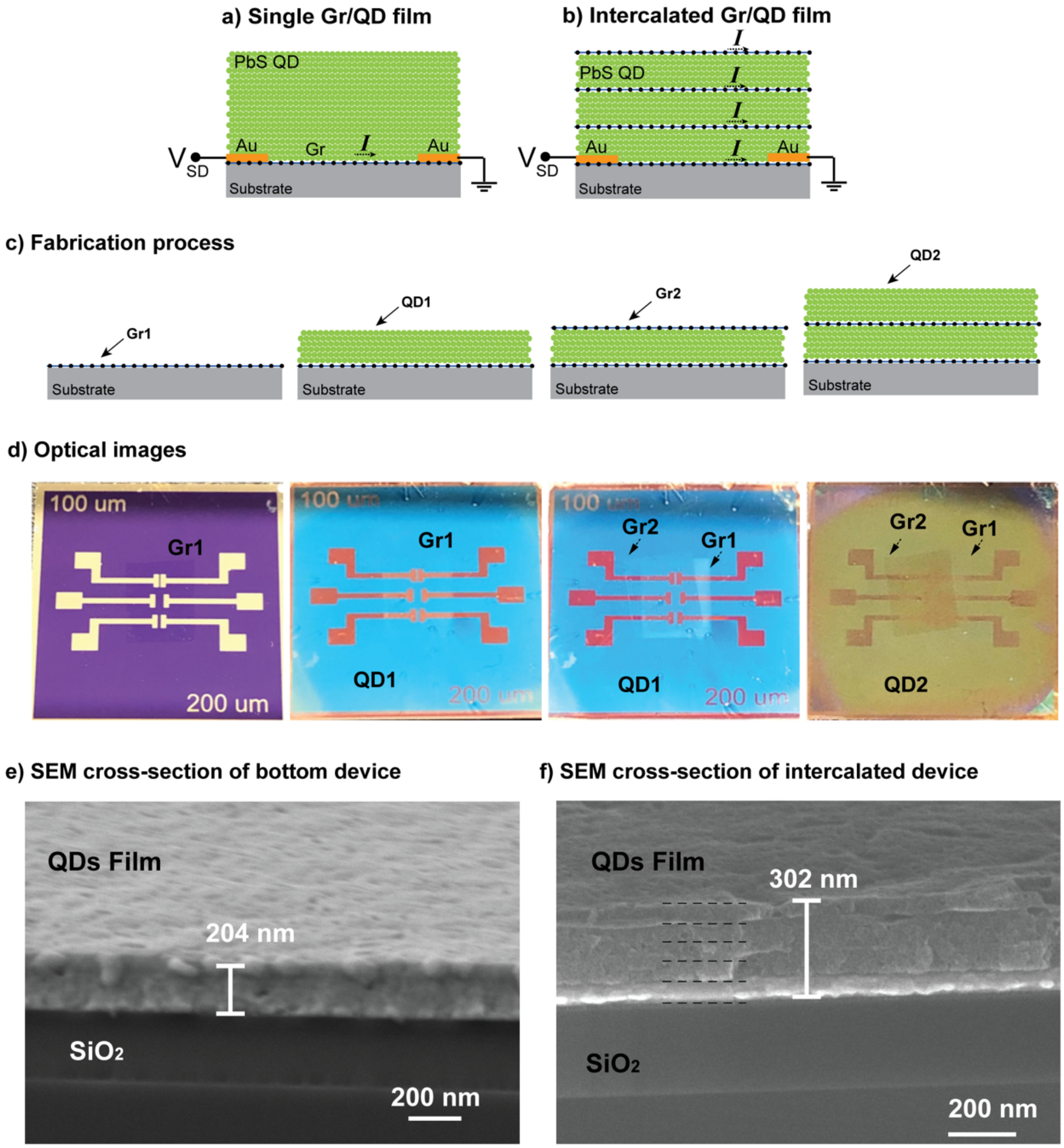

Figure 3.1 Intercalated devices and SEM cross-section images. a) Conventional hybrid Gr/QD dot device with single graphene layer at the bottom. b) Intercalated graphene layers in an intercalated Gr/QDs configuration enhancing charge collection and transport. c) Schematic of the sequential deposition of Gr and QD layers to realize intercalated devices. d) Optical images of an intercalated device at each step during fabrication process. e) Bottom Device consisting of a graphene followed with 10 layers of PbS QDs on top. The measured thickness of the film is ~204 nm. f) Intercalated Gr/QD devices fabricated by repeating the deposition of 1 layer of CVD graphene and 3 layers of PbS QDs sequentially into 5 stacks. The total measured thickness is ~302 nm, giving a measured graphene interspacing of $D_{Gr} \approx 302/5 = 60.4$ nm. From these results we assume that the thickness of each individual QD layer is ~20 nm. We neglect the contribution of graphene to the device thickness.

Our first analysis focuses on how light absorption evolves as QD and Gr layers are added sequentially, with each QD layer adding 20 nm in thickness. **Figure 3.2 a** shows the UV-Vis absorption spectra for the same device after adding each Gr and QD layer. The light absorption of the first Gr layer is negligible (black dashed line) due to the atomic thickness of graphene. After the first QD layer deposition, light absorption increases in the broad range from 450 nm to 1000 nm (red solid line). After adding the second Gr layer the absorption remains roughly the same since Gr has negligible absorption (red dashed line). Adding a second QD layer again increases light absorption (solid blue line) significantly, while adding another Gr layer (blue dashed line) has little effect. In the case of the Gr layer after the third QD layer (green dashed), there is a slight decrease in light absorption. **Figure 3.2 b** shows the evolution in light absorption at $\lambda = 650$ nm as QDs and Gr layers are added. Light absorption increases significantly only when QDs are added with minor absorption changes after Gr layers are added. These results confirm that graphene does not have a significant impact on the light absorption of PbS QD films.

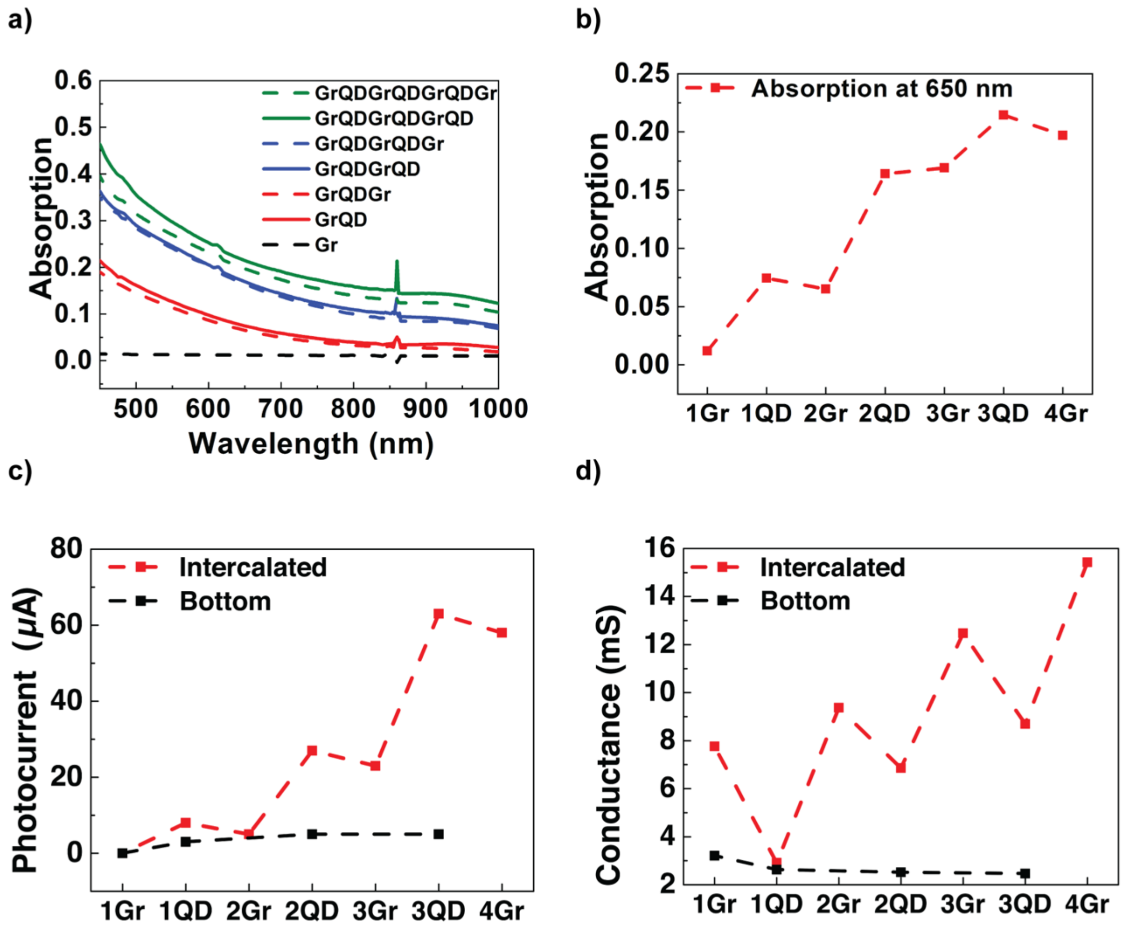

Figure 3.2 Light absorption, photocurrent (I_{ph}) and conductivity evolution in Gr/QD films. a) Light absorption of QDs films with intercalated graphene layers. The effect of adding graphene layers is minor compared with adding QD layers. b) Light absorption (λ =650 nm) evolution as Gr and QD layers are added, showing strong increment when QDs are added while Gr layers produce minor changes. c) Evolution of I_{ph} in intercalated devices show strong increments after adding QDs and minor reductions after adding Gr with an overall net increment as Gr and QDs are added. Bottom Gr device shows only a slight increase in I_{ph} after adding QD layers. d) Intercalated devices show increments in conductance after adding Gr layers with smaller but still significant reductions after adding QDs. As QDs and Gr layer are added there is a net increment in conductivity. Bottom Gr devices do not show significant changes as QDs are added. Photocurrent are measured under 532 nm laser diode, 0.9 mW.

A similar behavior can be observed in the evolution of the photocurrent ($I_{ph}=I_{light}$ - I_{dark}) for similar devices as shown in **Figure 3.2 c**. The red line shows the evolution for intercalated devices, whereas the black line represents reference devices with a single bottom graphene layer but same number of QD layers as intercalated devices. **Figure 3.2 c** shows that I_{ph} has major increments only after adding QD layers as more photons are absorbed and photocarriers are generated. It can also be observed that I_{ph} decreases slightly after Gr layers are added, but these setbacks are minor compared to the increments after adding QDs. For the non-intercalated devices (black line), I_{ph} slightly increased from 3 μA to 5 μA as the thickness of QDs increased from 1QD layer (t~20 nm) to 3QD layers (t~60 nm). In contrast, for intercalated devices, I_{ph} increased from 8 μA to 63 μA for 1QD layer (t ~20 nm) and 3QD layers (t ~60 nm).

The evolution in conductivity is shown in **Figure 3.2 d**. The black line shows the conductivity of a device only with a Gr bottom layer, remaining fairly constant when adding more QDs. This is expected because QD films have poor conductivity. In contrast, for the intercalated device (red line), the conductance increases after Gr layers are added, improving the film conductivity for intercalated devices. However, after adding QDs, the conductivity is significantly reduced. This can be due to transfer of electrons from QDs to Gr, which would reduce charge carrier concentration on typical p-type Gr. [91,131,132] The QDs can also affect the mobility and decrease the conductivity of Gr. Overall, the increase in conductivity by adding Gr layers is stronger than the negative effect of the QDs, as reflected on the overall increase in conductivity observed in **Figure 3.2 d**. The conductance of the intercalated device with 3QDs (t = 60nm) is 13.4 mS, whereas the bottom device with 3QDs stays low at 2.5 mS. Overall, the results in Figure 2 show that Gr has no major effect on light absorption of QD films, intercalated layers improve photocarrier collection, and adding Gr layers increase the overall conductivity of intercalated Gr/QD films.

3.3 Implement of Vertical Interconnect Access in Intercalated Architecture

3.3.1 Enhanced Charge Collection with VIAs Structure

Despite the improvements of intercalated films over bottom Gr devices, the short diffusion length, poor vertical conductivity, and the lack of vertical interconnects to Gr intercalated layers restrict the thickness of intercalated layers to ~200 nm.[129]

In order to increase light absorption for λ >650 nm radiation where light penetration depth in QDs is > 300 nm, QDs films with t > 300 nm devices are required. However, as the thickness increases, the photons absorbed in the top layers have a longer path to reach the bottom gold electrodes, reducing charge collection. To achieve thicker Gr/QD layers with efficient charge collection, we implemented two strategies: optimizing the distance between graphene layers (D_{Gr} in **Figure 3.3 a**), and implementing gold contacts as vertical interconnect access (VIAs) to graphene layers (**Figure 3.3 b**). Previous report on intercalated devices was based on one spin coating layer of QDs (D_{Gr} =20 nm) in between graphene layers.[129] However, it is known that QDs diffusion length (L_D) is around 50 nm to 200 nm.[98,101,102,133] Intercalated devices with D_{Gr} = 20 nm, 60 nm and 100 nm were fabricated, all stacked 4 times, resulting in thicknesses of t=80nm, 240 nm, and 400 nm, respectively. The light ON/OFF response under λ = 532 illumination for these devices is shown in **Figure 3.3 c**, showing the larger photoresponse for D_{Gr} = 60 nm. A plot of I_{ph} vs D_{Gr} for λ = 523 and 850 nm illumination as function of D_{Gr} (stacked 4 times, $t = 4\times D_{Gr}$) is shown in **Figure 3.3 e**. The plots clearly show that the D_{Gr} = 60 nm (t = 240 nm) device gives the highest I_{ph}. We infer that for D_{Gr} = 20 nm there is lower light absorption, reducing the photoresponsivity. For thicker devices with D_{Gr} = 100, 150, 200 nm (respective thickness of t = 400, 600, 800 nm) there is stronger light absorption, but the charge collection at the bottom gold contacts is poor, resulting in lower I_{ph}. Graphene interspacing of $D_{Gr} = 60$ nm offers the best compromise between light absorption and carrier collection.

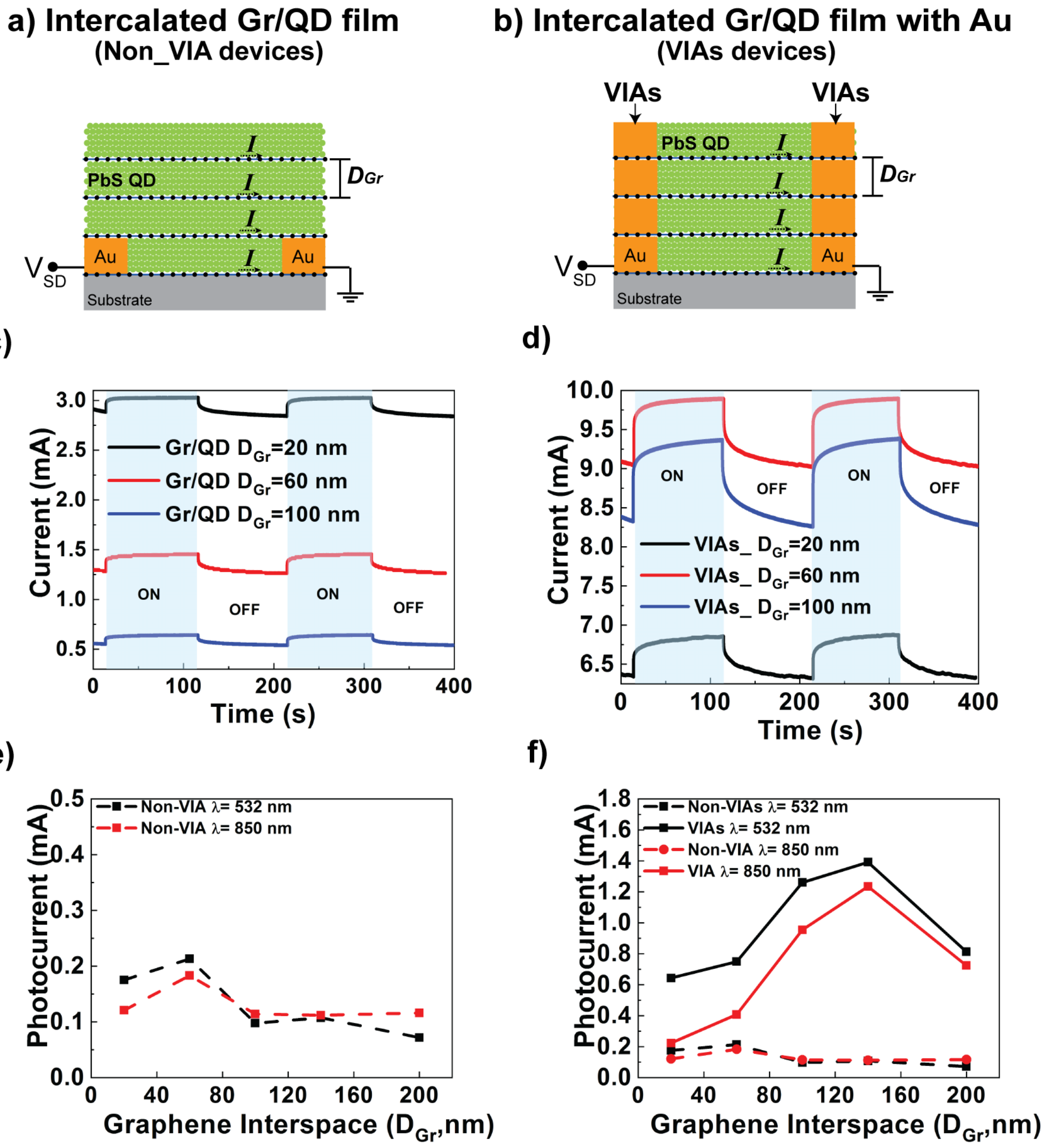

Figure 3.3 Graphene interspace (D_{Gr}) and Au VIAs. a) Device configuration of intercalated Gr/QD devices showing the graphene interspacing parameter D_{Gr} without VIAs. b) Device configuration with Au VIAs, connecting each Gr layer for enhanced charge collection. c) Light ON/OFF response for non-VIAs devices as shown in (a) with D_{Gr} = 20nm, 60nm, 100nm stacked 4 times with total thickness of t= 80nm, 240nm and 400nm respectively. ($\lambda = 532$ nm, $V_{DS} = 1$ V). d) Light ON/OFF response for Au VIAs devices as shown in (b) with D_{Gr} = 20nm, 60nm, 100nm stacked 4 times (t = 80nm, 240nm and 400nm respectively). The response of VIAs devices is stronger than the corresponding non-VIAs devices in c). e) I_{ph} vs D_{Gr} ($t = 4\times D_{Gr}$) under $\lambda = 532$ nm and 850 nm light for non-VIAs devices, showing highest response with D_{Gr} = 60 nm. f) I_{ph} vs D_{Gr} ($t = 4\times D_{Gr}$) under $\lambda = 532$ nm and 850 nm light for VIAs devices showing highest response with D_{Gr} = 160 nm. Measurements are under 532 nm (0.9 mW) and 850 nm (3.5 mW) laser diode illumination.

The most important improvement to overcome the poor vertical transport and reach thicker QDs film is the implementation of gold contacts that serve as vertical interconnect access (VIAs) to each Gr layer, as shown in **Figure 3.3 b**. Charges collected at any Gr layer will be fully collected through the VIAs. The ON/OFF photoresponse for VIAs devices with D_{Gr} = 20 nm, 60 nm and 100 nm is shown in **Figure 3.3 d**. Comparing VIAs devices in **Figure 3.3 d** with non-VIAs devices in Figure 3c with same D_{Gr} and thickness shows that VIAs devices have a much higher I_{ph} that we attribute to enhanced current collection through the gold interconnects. **Figure 3.3 f** shows I_{ph} vs D_{Gr} ($t = 4 \times D_{Gr}$) under $\lambda = 532$ nm and 850 nm illumination, both for VIAs and non-VIA devices, showing that VIAs devices have a stronger response for any D_{Gr}. In contrast to non-VIAs devices, VIAs show a stronger I_{ph} for $D_{Gr} = 140$ nm than for $D_{Gr} = 60$ nm, indicating the efficient collection through the Au contacts. It is also important to point that VIAs devices show increased response for both $\lambda = 532$ nm and $\lambda = 850$ nm (NIR) illumination. The VIAs structures therefore allow building thicker devices while keeping efficient charge collection.

The improved performance of VIAs over non-VIAs devices over a range of light intensity is shown in **Figure 3.4 a**. The increase in responsivity as function of light intensity has been reported for previous Gr/QD hybrid devices and is due to higher recombination rate, reduced built-in potential, and saturation of sensitizing traps in QDs as power increases.[66,91,134,135] Despite the intercalated configuration, an electrostatic back gate is still capable of modulating carrier concentration in graphene layers. **Figure 3.4 b** shows I_{DS} vs V_G in light and dark conditions. In both cases, there is a clear signature of graphene, showing ambipolar conductivity, hitting a minimum when the Fermi level is at the Dirac point. In both cases the Dirac point is located at $V_G > 0$ as well, indicating that the Fermi level is below the Dirac point in the valence band (p-doped). It is also clear that from dark to light there is a clear shift in the position of the Dirac point, shifting from V_G = 65 V in dark to V_G = 78 V under illumination, indicating a down shift in Fermi level and therefore a transfer of holes from the QDs to Gr under illumination. The transfer of holes to p-doped results in increase conductivity. **Figure 3.4 c** plots I_{ph} vs V_G, demonstrating that the light response can be tuned with the back gate, allowing to even get a negative I_{ph} for $V_G > 70$ V.

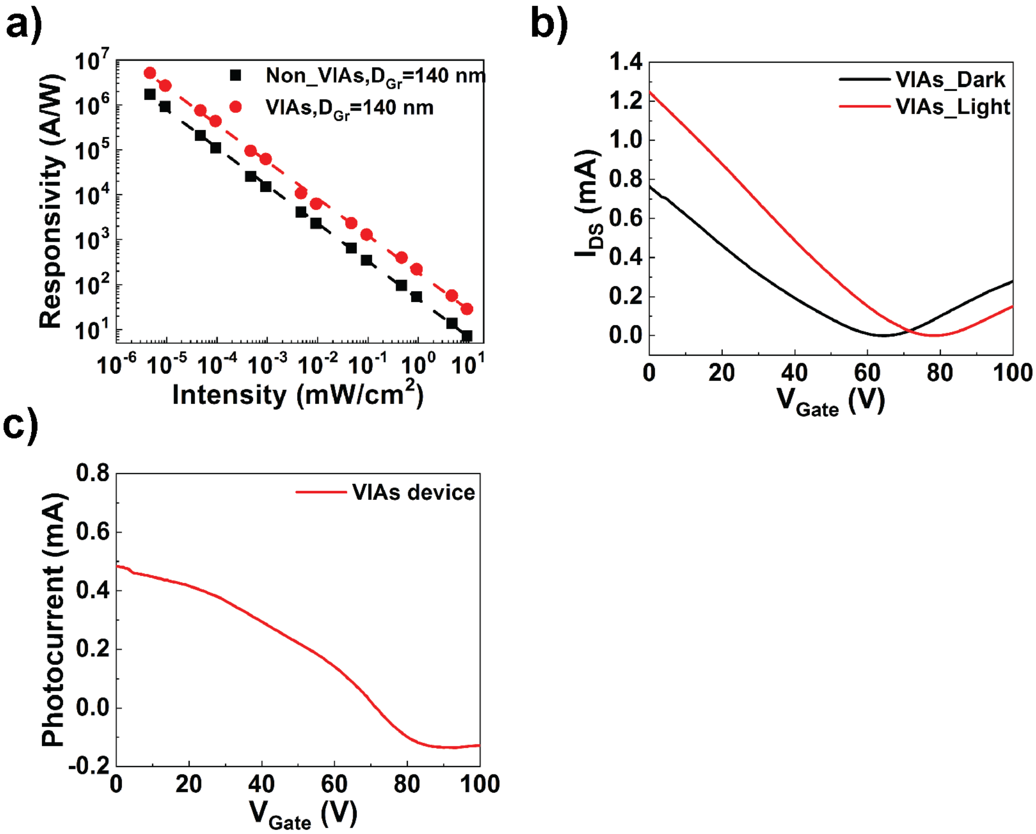

Figure 3.4 Light response dependence on intensity and gate voltage. a) Responsivity increases as incident power decreases. VIAs device shows superior performance than non-VIAs devices across different intensities. b) I_{DS} vs V_G in light and dark conditions for VIAs devices showing ambipolar graphene conductivity reaching the Dirac peak at V_G = 65 V in dark and V_G = 78 V in light. c) I_{ph} vs V_G for VIAs device, showing that photoresponse can be modulated through a gate voltage, reaching negative response for V_G >71.6 V. In all cases the device has D_{Gr} =140 nm and t = 560 nm.

3.3.2 VIAs Device Fabrication

The hybrid photodetector used monolayer CVD graphene from Graphenea and PbS quantum dots from CANdots (Germany) with fluorescence at λ_{em}= 1000 nm. Photolithography was used to define the electrode pattern on SiO_2/Si (285 nm/500 μm) substrate. Chromium/gold (10 nm/100 nm) was evaporated to form the electrodes with device dimension of 100 μm channel length and 800 μm channel width. Graphene was transferred onto the substrate by PMMA wet-transfer. PbS QDs films were deposited using spin-coating under ambient atmosphere. For each PbS QDs layer, the QDs solution (30 mg/mL in toluene) was spin coated at 2500 rpm for 30s, then a solid-state ligand exchange was performed by flooding the surface with 0.03 M TBAI in methanol for 30s before spinning dry at 2500 rpm. For the bottom Gr/QD system, QDs film was formed layer-by-layer. The intercalated devices were realized by alternating graphene transfers with spin-coating of QDs films. For the VIAs devices, QDs were etched partially, then chromium/gold (10 nm/100 nm) were deposited by e-beam evaporator, and Gr transfer QDs spin coating were carried out sequentially.

3.4 Conclusion

In conclusion, we have demonstrated the complementary role that Gr and QDs play in intercalated Gr/QD photodetectors and improved their performance by optimizing the graphene interspacing and adding gold contact VIAs on each graphene layer. The graphene layers have a minor impact on the light absorption of QD films and contribute to efficient charge collection of photocarriers produced by the QDs. The optimization of the graphene interspacing also allows for thicker films while keeping efficient charge collection. The intercalated Gr/QDs with VIAs show enhanced performance compared to conventional intercalated structure. The VIAs system helps to improve charge carrier collection and overcome the poor vertical conductivity, breaking the limitation of QDs film thickness in optoelectronic devices. This optimal intercalated Gr/QDs system with VIAs Au contacts can be the route to achieve thicker QDs film (t >500 nm) enabling much stronger photoresponsivity and quantum efficiency for NIR light detection and showing potential for improved photovoltaic conversion using intercalated charge collectors.

Chapter 3, in full, is a reprint of the material as it appears in “Implementation of Metallic Vertical Interconnect Access in Hybrid Intercalated Graphene/Quantum Dot Photodetector for Improved Charge Collection”. Chen, Wenjun; Ahn, Seungbae; Rangel, Carlos; Vazquez-Mena, Oscar. Frontiers in Materials. 6, 1-7 (2019). The dissertation author was the primary investigator and author of this paper.

Chapter 4 1-μm Thick QDs Films with Near Full Light Absorption and Charge Collection

4.1 Introduction

Quantum dots (QDs) offer several advantages in optoelectronics such as easy solution processing, strong light absorption and size tunable direct bandgap. However, their major limitation is their poor film mobility and short diffusion length (< 250 nm). This has restricted the thickness of QD film to ~200-300 nm due to the restriction that the diffusion length imposes on film thickness in order to keep efficient charge collection. Such thin films result in a significant decrease in quantum efficiency for λ >700 nm in QDs photodetector and photovoltaic devices, causing a reduced photoresponsivity and a poor absorption towards the infrared part of the sunlight spectrum. Herein, we demonstrate 1 μm thick QDs photodetectors with intercalated graphene charge collectors that avoid the significant drop of quantum efficiency towards λ >700 nm observed in most QD optoelectronic devices. The 1 μm thick intercalated QD films ensure strong light absorption while keeping efficient charge extraction with a quantum efficiency of 90%–70% from λ = 600 nm to 950 nm using intercalated graphene layers as charge collectors with interspacing distance of 100 nm. We demonstrate that the effect of graphene on light absorption is minimal. We achieve a time-modulation response of ~1 s. We demonstrate that this technology can be implemented on flexible PET substrates, showing 70% of the original performance after 1000 times bending test. This system provides a novel approach towards high-performance photodetection and high conversion photovoltaic efficiency with quantum dots and on flexible substrates.

Photodetection and photovoltaic devices are of great relevance for a variety of applications, such as optical communications, imaging, sensing and harvesting. Beyond the visible region, the near-infrared (NIR) is especially important in night vision, medicine and other photodetection devices.[137,138] Similarly, a significant part of the sunlight spectrum is in the NIR, contributing with a significant number of photons that for single junction photovoltaic cells give the same contribution as visible photons. Quantum dots (QDs) have emerged as promising materials for photodetection and photovoltaics due to their easy and low cost synthesis and solution processing, and their high-quality optoelectronic properties such as strong light absorption and size tunable direct bandgap.[139,140] However, the short diffusion length in QDs films ($L_D < 250$ nm) limits their useful thickness to ~200-300 nm;[100,101,133,141] this is a result of the well-known compromise between light absorption and diffusion transport charge extraction in QDs films. Visible photons have a penetration depth < 200 nm, therefore they are effectively absorbed by ~300 nm thick QD films. However, in the near-infrared range, the penetration depth increases drastically to >300 nm and thin QD films t ~250 nm cannot capture NIR light efficiently (penetration depth shown in Chapter 2 **Figure 2.2 b**). This results in a significant drop of quantum efficiency (EQE) starting at λ ~700 nm that is present in several top performing solar cells reported recently.[27,100,101,103] This is a consequence of their short L_D limiting the QD film thickness ($t < 300$ nm). Similarly, QD and hybrid QD/2D photodetectors show a drop in photoresponsivity as light wavelength increases towards the NIR range,[58,94,116] limiting the performance of QDs optoelectronics in the NIR range.

Herein we report ultra-thick QD photodetector films reaching 1-micron thickness for enhanced light absorption, while maintaining high charge extraction efficiency by utilizing multiple intercalated graphene (Gr) monolayers with gold vertical interconnect access (VIAs) contacting each graphene layer. Important reviews on QD optoelectronics suggest that ~1-micron thick QD films are required to efficiently absorb sunlight in photovoltaic devices.[35,38,68] We show the increase in light absorption as function of thickness, showing a limited effect of the graphene intercalated layers on light absorption. The improved performance of intercalated vs non-intercalated (bottom devices) under time modulated light is also shown. We study how the interspacing distance between graphene layers (D_{Gr}) affect the performance of the devices. Then, we study photoresponsivity and show the superior EQE of 1-micron thick QD devices reaching near 90%–70% EQE from λ = 600 to 950 nm, avoiding the drop in performance at λ ~700 nm observed in previous reports of QD devices.[27,100,101,103] Finally, we show that the same structure can be implemented on flexible devices showing superior photoresponsivity.

4.2 Study of Hybrid QDs/Gr Structure and Gr Interspacing

Diagrams illustrating the architecture and operation of bottom and intercalated hybrid Gr/QDs photodetectors are shown in **Figure 4.1 a** and **b**. The intercalated devices are fabricated by sequential and alternating spin coating of PbS QDs with bandgap E_g = 1.18 eV (1050 nm) and wet transfer of graphene monolayers. In Gr/QDs hybrid system, photogenerated holes are transferred to graphene and driven by a bias voltage to produce photocurrent, while photogenerated electrons stay in QDs causing a photogating effect. In the case of bottom devices, only carriers generated within the diffusion length from the bottom contact can be efficiently transferred to graphene, whereas for intercalated layers the carriers can be collected at any point in the film as long as $L_{\mathrm{D}} > D_{\mathrm{Gr}}$.[58,91] **Figure 4.1 c** and **d** show SEM cross section images of bottom and intercalated devices 800 nm thick. The intercalated devices have a graphene interspacing of D_{Gr} = 100 nm, with a clear layered structure. **Figure 4.1 e** shows the light absorption spectra of QD films with thickness t = 200 and 400 nm with bottom and intercalated graphene layers showing the characteristic exciton absorption peak at λ ~1050 nm. Evidently, thicker films have stronger absorption, but more importantly, the intercalated and bottom devices show similar absorption spectra, indicating that the graphene intercalated layers do not have a significant or degrading effect on the QD absorption. In contrast, intercalated devices have a much higher photoresponse than bottom devices, as shown in the time photoresponse under λ = 850 nm illumination in **Figure 4.1 f**. The improvement in photoresponse is more pronounced for the 400 nm than for the 200 nm thick device. The photocurrent of intercalated devices are 112 μA (t = 200nm) and 148 μA (t = 400nm), while for the bottom devices are 75 μA (t = 200nm) and 57 μA (t = 400nm), indicating that intercalated graphene layers improve photoresponse by enhancing the charge collection.

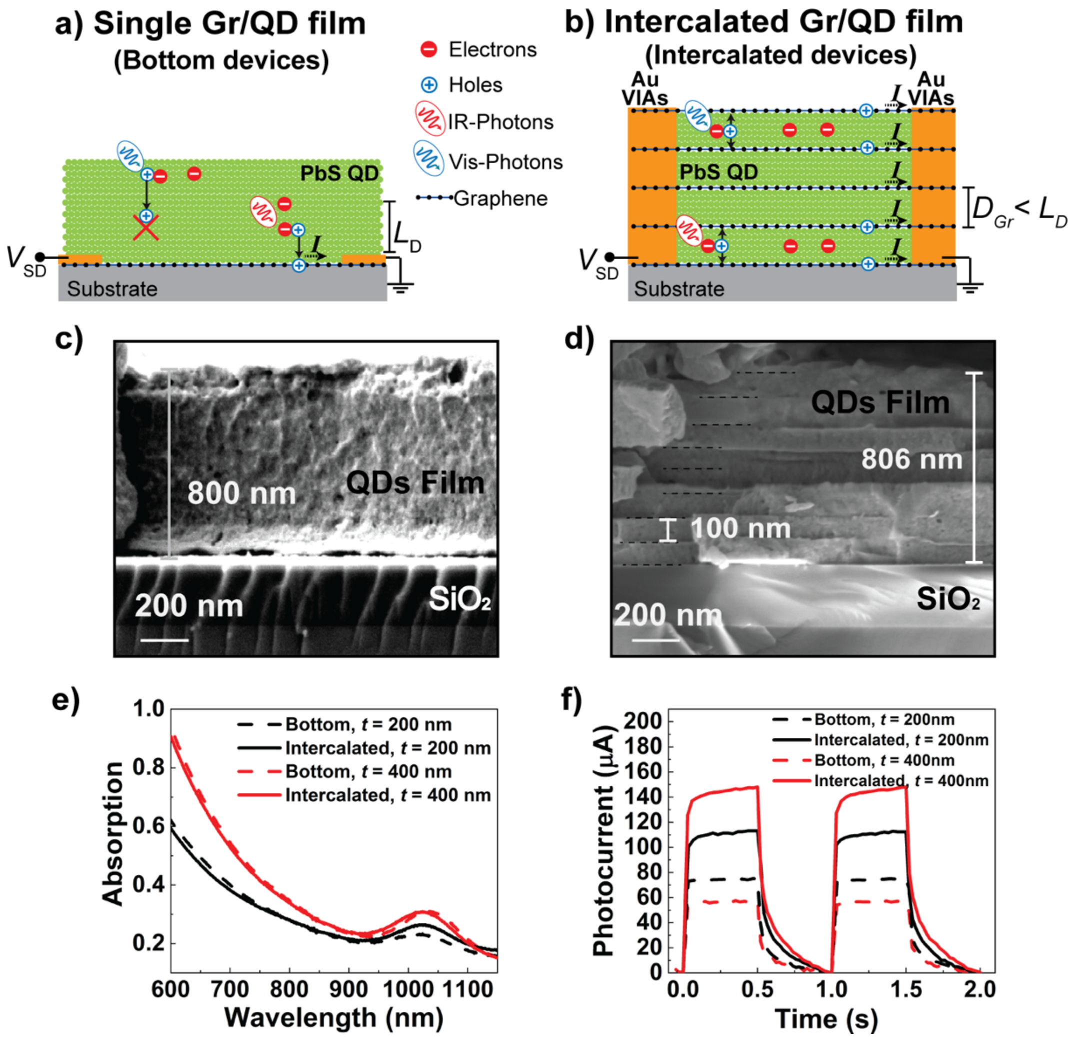

Figure 4.1 Bottom and intercalated devices. Schematic images of a) conventional hybrid Gr/QDs device with single graphene at the bottom (Bottom devices), and b) intercalated configuration with Au VIAs for enhanced charge collection. SEM images of c) bottom device and d) intercalated device both with total QDs film thickness of 800 nm. e) Light absorption spectra of 200 and 400 nm thick devices, showing no significant difference between bottom and intercalated devices. f) Photocurrent response of 200 and 400 nm thick devices, showing stronger response of intercalated over bottom devices. Measurements were performed using laser excitation at $\lambda = 850$ nm and $V_{DS} = 1$ V.

A critical parameter in intercalated devices is the graphene interspacing (D_{Gr}), which should be smaller than the diffusion length L_D to keep efficient charge collection. At the same time, D_{Gr} should not be so small to the point of making the fabrication process extremely long by requiring too many graphene transfers. The first reported intercalated devices had $D_{Gr} = 20$ nm,[124] which would require an impractical number of 50 intercalated layers for a 1-micron thick layer. In order to study the effect D_{Gr}, we fabricated 800 nm thick intercalated devices with varying spacings of $D_{Gr} = 100$, 133, 166, and 200 nm, which means 9, 7, 6, and 5 graphene layers, respectively, where the number of layers is $\#L = t/D_{Gr} + 1$. **Figure 4.2 a** shows the absorption spectroscopy of the $t = 800$ nm films with different D_{Gr} showing no significant differences. The limited effect of Gr on the absorption of intercalated films has been reported in intercalated QD/Gr devices.[124,136] However, the photoresponsivity does show significant changes with D_{Gr} as shown in **Figure 4.2 b** and **c**. The intercalated device with $D_{Gr} = 100$ nm gives the best photocurrent ($I_{ph} = I_{light} - I_{dark}$) with lower response for larger D_{Gr}. It is possible that $D_{Gr} < 100$ nm can give higher responsivity, however, the number of graphene layers required would make it impractical. From these results, we fix $D_{Gr} = 100$ nm to build intercalated films up to 1-micron in thickness.

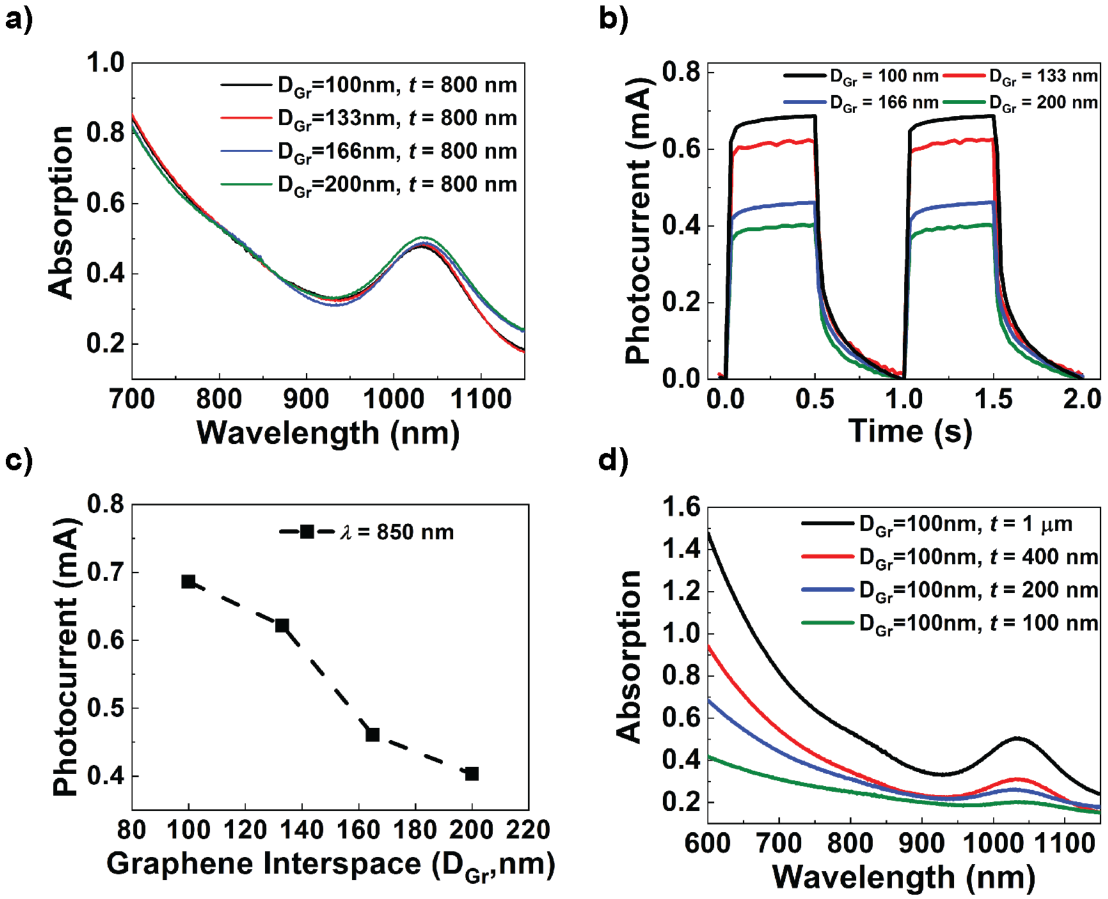

Figure 4.2 Effect of graphene interspacing (D_{Gr}) in intercalated devices. a) Absorption of intercalated QD films with D_{Gr} = 100 nm, 133 nm, 166 nm, and 200 nm and total thickness t = 800 nm. The effect of graphene is limited on light absorption. b) Light ON/OFF response for intercalated devices with different D_{Gr} and total thickness of t = 800 nm. D_{Gr} = 100nm gives the best light response with charge extraction decreasing for $D_{Gr} > 100$ nm. c) Plot of photocurrent as function of D_{Gr}. Measurements were performed using laser excitation at λ = 850 nm and V_{DS} = 1 V. d) Light absorption spectra of QDs films mentioned in Figure 4.4, intercalated with graphene at D_{Gr} = 100 nm.

a) t = 100 nm, D_{Gr} = 100 nm; τ_{fast} = 0.08 s and τ_{slow} = 4.36 s.

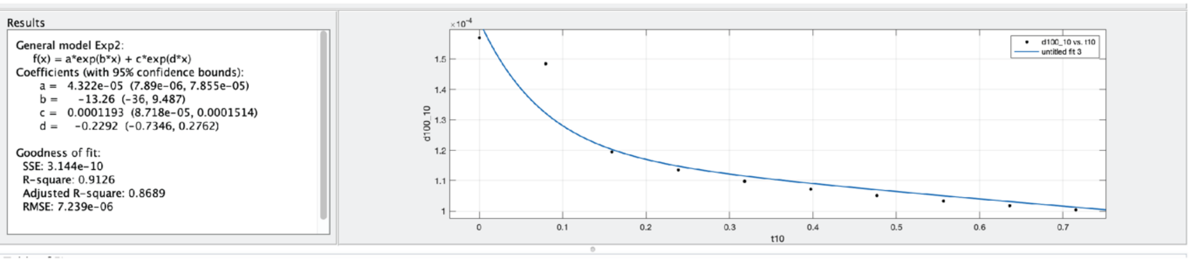

```
Results
General model Exp2:
    f(x) = a*exp(b*x) + c*exp(d*x)
Coefficients (with 95% confidence bounds):
      a =   4.322e-05  (7.89e-06, 7.855e-05)
      b =      -13.26  (-36, 9.487)
      c =   0.0001193  (8.718e-05, 0.0001514)
      d =     -0.2292  (-0.7346, 0.2762)

Goodness of fit:
  SSE: 3.144e-10
  R-square: 0.9126
  Adjusted R-square: 0.8689
  RMSE: 7.239e-06
```

b) t = 200 nm, D_{Gr} = 100 nm; τ_{fast} = 0.07 s and τ_{slow} = 4.17 s.

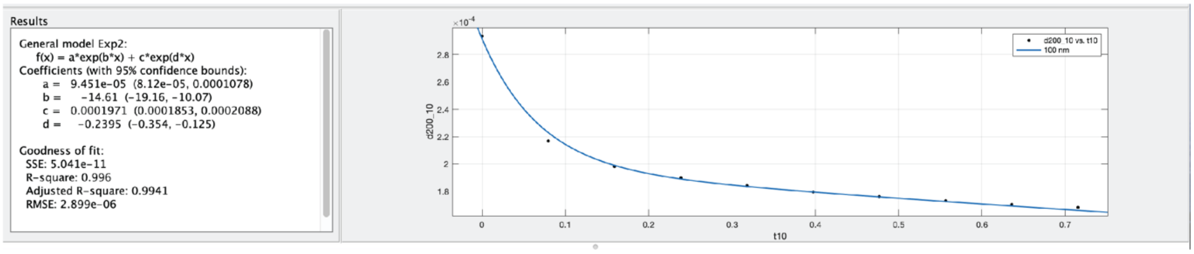

```
Results
General model Exp2:
    f(x) = a*exp(b*x) + c*exp(d*x)
Coefficients (with 95% confidence bounds):
      a =   9.451e-05  (8.12e-05, 0.0001078)
      b =      -14.61  (-19.16, -10.07)
      c =   0.0001971  (0.0001853, 0.0002088)
      d =     -0.2395  (-0.354, -0.125)

Goodness of fit:
  SSE: 5.041e-11
  R-square: 0.996
  Adjusted R-square: 0.9941
  RMSE: 2.899e-06
```

c) t = 400 nm, D_{Gr} = 100 nm; τ_{fast} = 0.08 s and τ_{slow} = 4.35 s.

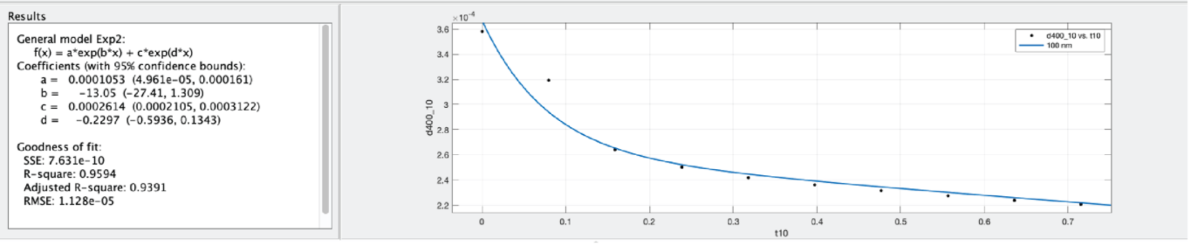

```
Results
General model Exp2:
    f(x) = a*exp(b*x) + c*exp(d*x)
Coefficients (with 95% confidence bounds):
      a =   0.0001053  (4.961e-05, 0.000161)
      b =      -13.05  (-27.41, 1.309)
      c =   0.0002614  (0.0002105, 0.0003122)
      d =     -0.2297  (-0.5936, 0.1343)

Goodness of fit:
  SSE: 7.631e-10
  R-square: 0.9594
  Adjusted R-square: 0.9391
  RMSE: 1.128e-05
```

d) t = 1000 nm, D_{Gr} = 100 nm; τ_{fast} = 0.07 s and τ_{slow} = 3.18 s.

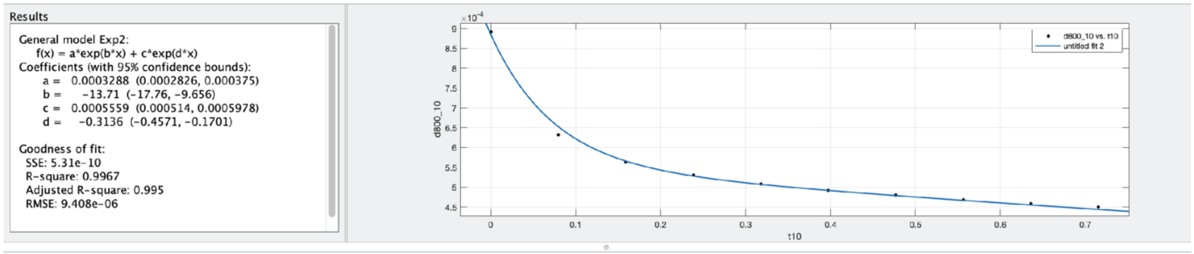

```
Results
General model Exp2:
    f(x) = a*exp(b*x) + c*exp(d*x)
Coefficients (with 95% confidence bounds):
      a =   0.0003288  (0.0002826, 0.000375)
      b =      -13.71  (-17.76, -9.656)
      c =   0.0005559  (0.000514, 0.0005978)
      d =     -0.3136  (-0.4571, -0.1701)

Goodness of fit:
  SSE: 5.31e-10
  R-square: 0.9967
  Adjusted R-square: 0.995
  RMSE: 9.408e-06
```

Figure 4.3 Time constants. Carrier lifetime extracted from the fitting to two-components exponential decay of different thickness a) t = 100 nm, b) t = 200 nm, c) t = 400 nm, d) t = 1000 nm, two time constants τ_{fast} and τ_{slow} as reported previously.[58,91]

The time response of the devices shows a fast and slow component as shown in **Figure 4.3**, as observed previously in first Gr/QD hybrid devices.[58] The fast components is ~70 ms, allowing for sub-second light modulation shown in **Figure 4.2 b**. We do not observe major variations in time response for different D_{Gr}. The slow component of the time response is ~3 second, which is responsible for the large photogain of the devices analyzed as followed. This long lifetime is probably associated to traps in the QDs.

Photogain *(G)*

$$G = \frac{\tau_{lifetime}}{\tau_{transit}} = \frac{\tau_{lifetime}}{L^2}\mu\, V_{DS} \qquad \text{Equation 4.1}$$

Using L = 1 mm, μ_h~400 cm^{2}V^{-1}s^{-1}, V_{DS} = 10 mV and $\tau_{lifetime}$ = 3.1 sec

$$G = 1.33 \times 10^3 \qquad \text{Equation 4.2}$$

External Quantum Efficiency (*QE*)

$$EQE = R\frac{hc}{q\lambda}\frac{1}{G} \qquad \text{Equation 4.3}$$

This expression is used to obtain EQE in Figure 3.c from R in Figure 3.b using $G = 1.33 \times 10^3$ Equation 4.4

We use the long lifetime since the data for R was obtained with an integration time of 15 s. The high photogain is also associated with long lifetime in QDs in the order of ~1 sec due to traps in the QDs.

4.3 1-μm Thick QDs Films

Figures 4.4 a and **b** show the spectral photoresponsivity ($R = I_{ph}/P_{inc}$, $I_{ph} = I_{Light} - I_{Dark}$) of bottom and intercalated (D_{Gr} = 100 nm) devices with t = 100, 200, 400 and 1000 nm. **Figure 4.4 a** shows that for bottom devices, t = 200 nm shows the best performance, keeping efficient charge collection. Thicker $t = 400$ nm and 1 μm thick films give lower responsivity. However, it is worth pointing out that the 1 μm film shows better performance than $t = 100$ and 400 nm in the $\lambda =$ 900−1100 nm, probably due to the infrared photons being absorbed deeper and near to the bottom Gr/QD interface. The intercalated devices in **Figure 4.4 b** show a drastic improvement over their corresponding bottom devices. Furthermore, R increases as the thickness increases from 100 nm to 1 μm across the entire spectrum, indicating efficient charge collection as thickness increases. It is also important to point out that for $t = 100$, 200 and 400 nm intercalated devices, R increases up to λ ~700 nm, but then R decreases as longer wavelengths have deeper penetration depths. In contrast, the 1-micron thick device shows a clear increase in responsivity up to λ ~900 nm. This behavior marks an important contrast with previous hybrid PbS/Gr and PbS/MoS_2 devices with bottom 2D material, which show a clear decrease in responsivity from $\lambda = 600$ nm towards $\lambda =$ 1000 nm.[58,116,117,123] The light absorption spectrum of the same intercalated films is shown in supporting information in **Figure 4.2 d**. The quantum efficiency can be extracted by estimating the photogain[119] as shown in previous section. Using $L = 1$ mm, μ_h ~400 $cm^2V^{-1}s^{-1}$, $V_{DS} = 10$ mV and $\tau_{lifetime} = 3.1$ s, we obtain a photogain of $G = 1.2 \times 10^3$. The QE is obtained from $R = (QE)G(\frac{q\lambda}{hc})$ and is plotted in **Figure 4.4 c**, reflecting the improved charge collection as thickness increases beyond the diffusion length (L_D ~100-200 nm), breaking its restriction on the film thickness. The QE of the 1μm thick device keeps at 70% −90% from $\lambda = 600$ nm to 950 nm, avoiding the drastic drop at $\lambda = 700$ nm. Up to our knowledge, this is the first report with a PbS-QD optoelectronic devices having such high EQE avoiding the drop of performance near λ ~700 nm. The high charge collection achieved from $\lambda = 600$ nm to 950 nm is remarkable for a QD film. We remark that our intercalated and bottom devices show low performance at λ ~500 nm, which can be due to degradation by device fabrication in air and the Gr transfers in aqueous solutions. Some reports show significant degradation of PbS-QD devices in the visible range after air exposure.[27,142,143] This can eventually be corrected by implementing the fabrication process in a glove box and using Gr dry transfers. Further confirmation of the superior performance of intercalated devices is shown in **Figure 4.4 d,** showing *R* as function of light intensity with a □ = 850 nm laser. Over the power intensity range of 10^{-5} to 10^{1} mWcm^{-2}, the 1-micron thick device has a 2-orders of magnitude improvement in photoresponsivity over the 1-micron thick bottom device. The decrease in responsivity as light intensity (P_{inc}) increases reflects the $R \sim P_{\mathrm{inc}}^{\beta-1}$ ($\beta<1$) behavior of Gr/QD photodetectors,[91] observed in several QD photodetector reports.[58,91,117,124] This behavior is mainly due to lower lifetime as light intensity increases, reducing the photogain.

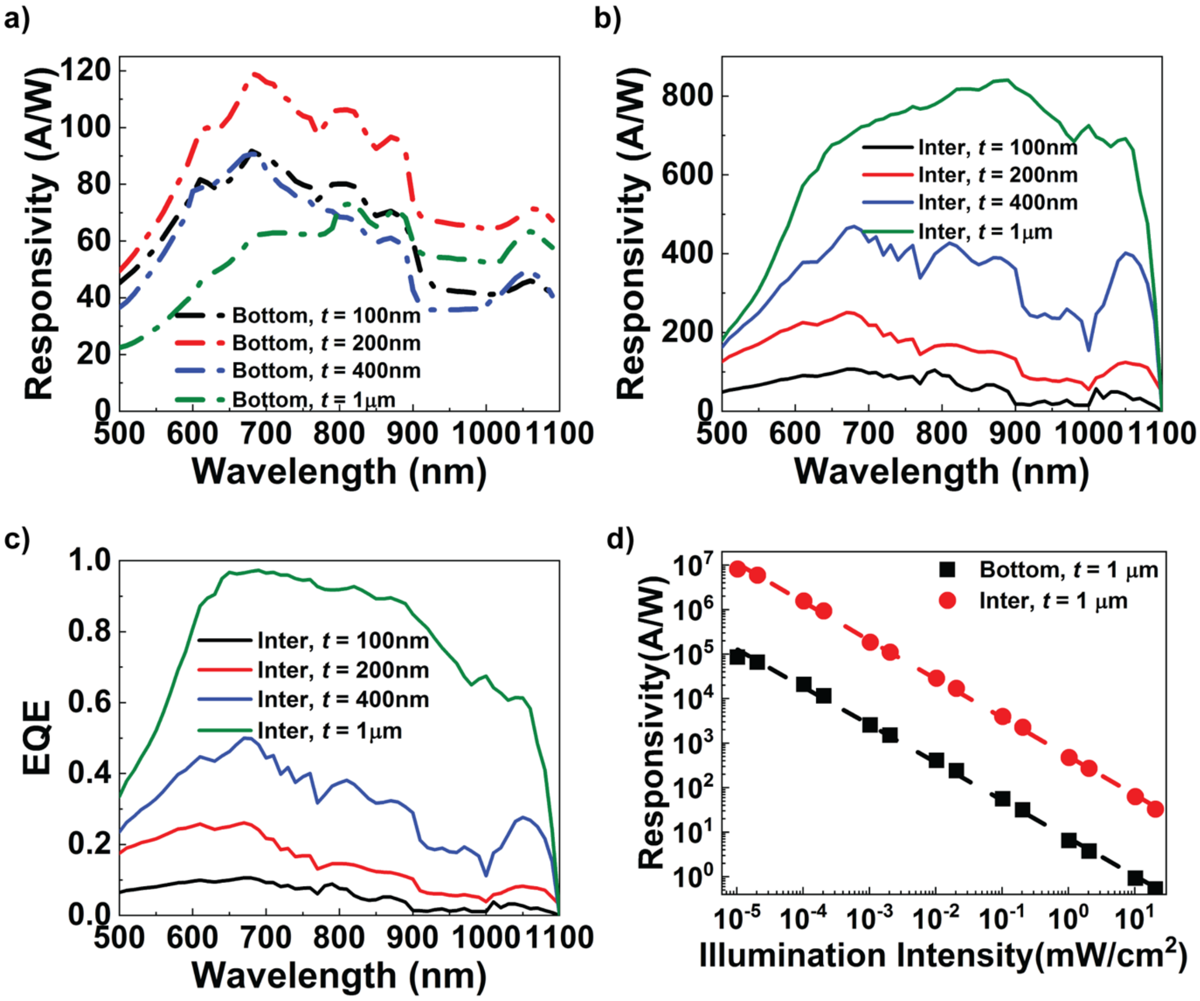

Figure 4.4 Spectral response. a) Spectral responsivity ($R = I_{ph} / P_{inc}$) for bottom devices with different thickness under 10 mV bias. Highest R is obtained at $t = 200$ nm, which ensures efficient charge collection. b) Responsivity for intercalated devices, showing that R increases as thickness increases from 100 nm to 1 μm over the entire spectrum. Only the 1-micron thick device keeps R increasing in the $\lambda \sim 600–900$ nm range. c) EQE increases across spectrum for intercalated devices as t increases. Whereas $t = 100–400$ nm devices show a drop in EQE at $\lambda = 700$ nm, the 1 μm thick device keeps EQE without significant drop from 600 nm to 900 nm. d) R increases as light intensity decreases. Intercalated device shows two orders of magnitude higher R than bottom device. Devices in d) are under $V_{SD} = 5$ V and 850 nm laser excitation.

4.4 Flexible Substrate Compatibility

Gr/QD intercalated devices can be easily fabricated and implemented on flexible substrates. CVD-grown single layer graphene and QDs were sequentially deposited on a polyethylene terephthalate (PET) substrate. **Figure 4.5 a** shows the optical image of the PET substrate with

Gr/QD intercalated film. **Figure 4.5 b** and **c** show the light response of the flexible VIAs device (t = 600 nm) under 850 nm light irradiation before and after a bending test for 1000 times, showing up to 70% degradation in response after 1000 bending cycles. Therefore, intercalated devices can be easily applied onto flexible substrate for wearable sensing, imaging and other optoelectronic applications.

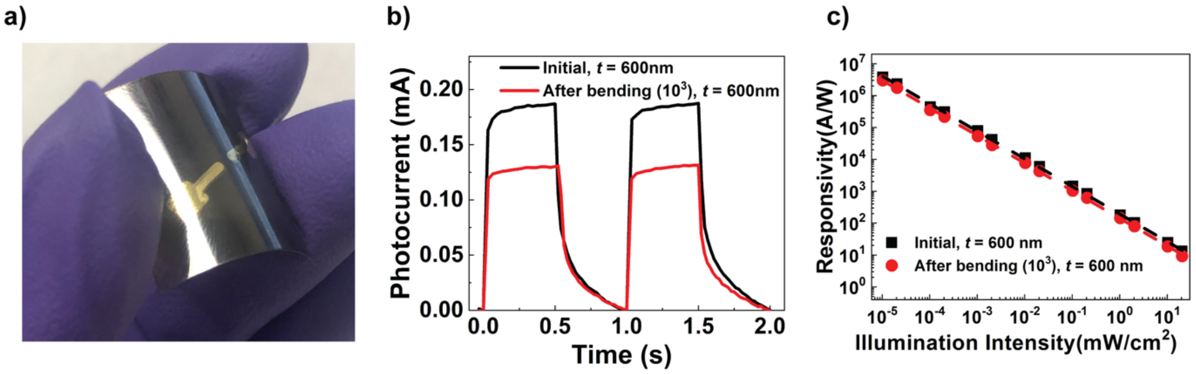

Figure 4.5 Responsivity of intercalated device on flexible PET substrate. a) Optical image of QDs and graphene intercalated device on PET substrate, QDs thickness t = 600 nm. b) Light response of device in (a) before and after a bending test for 1000 times under 1 V bias, λ = 850 nm P_{inc} = 3.5 mW. c) Responsivity of the flexible VIAs device as a function of incident light intensity characterized before and after bending test under 5 V bias, λ = 850 nm laser diode.

4.5 Conclusions

The 1-μm intercalated QD films herein presented achieve improved photodetection exhibiting high EQE~70-90% across the λ = 600–950 nm range without the typical drop near λ ~700 nm observed in top/bottom QD photodetectors and photovoltaic cells. The intercalating graphene layers using VIAs allows efficient charge collection despite the total QDs film thickness, breaking the restriction that short diffusion length imposes on the thickness of QDs films. The intercalated configuration herein presented has a direct application to improve broadband spectrum detection towards the infrared using Gr/QD. Recently, the integration of Gr/QD with CMOS has shown the power of this hybrid technology for broad spectrum imaging.[144] In order to push

Gr/QD/CMOS detection technology towards longer wavelengths with deeper penetration depths, thicker QD films can be required, in which case, intercalated films can be the perfect tool to improve photon capture keeping charge collection.

Another exciting but more challenging path forward is to apply the intercalated architecture to photovoltaic cells intercalating QDs with n- and p-type intercalated layers, such as MoS_2 (n-type)[117,123] and Gr (p-type), allowing to separate both electrons and holes to obtain a photovoltaic cell. State-of-the-art solar cells (*t* ~250 nm) from leading groups in QDs typically show high EQE~80% in the λ ~400−700 nm range, with strong decline to 50% in the λ ~700−1000 nm range as shown in **Figure 4.6**. They show a drastic drop in EQE around λ ~600-700 nm. The area under the curve represents photons used (absorbed and photocarriers collected) and the area over the curve represents photons wasted. Ideally, EQE would be 100% from λ ~400−1100 nm, representing full absorption and collection of photons with energy above the band gap. The dashed diagonal are just eye-guides from EQE: 100% to $\lambda = 1100$ nm, splitting the photocarrier collection in two halves: 50% collected, 50% wasted. As seen in all the figures below, QD solar cells only collect and use 50-60% of photons, while 50-40% are wasted due to poor collection in the λ = 600−1000 nm range. For single junction devices, each photon contributes equally to the photovoltaic power. Intercalated devices offer a path to achieve EQE ~90−100% up to λ ~1000 nm, which would allow capturing the photons that are currently wasted (~40-50%), which would be a route to improve current conversion efficiencies in the 9−13% towards 20%.

This means that about 50-40% of the total incident photons in the λ ~400−1000 nm range are not captured, mainly in the λ ~700−1000 nm range. Improving EQE to ~95% in the entire λ ~400−1000 nm range would represent collecting almost the entire sunlight photon influx above the bandgap, potentially boosting the photovoltaic performance of QD solar cells from the current 10-15% range[100–102,145] towards 20%. 1-micron thick QDs films with intercalated electrodes represent a potential path forward to achieve 20% efficiencies with QD solar cells.

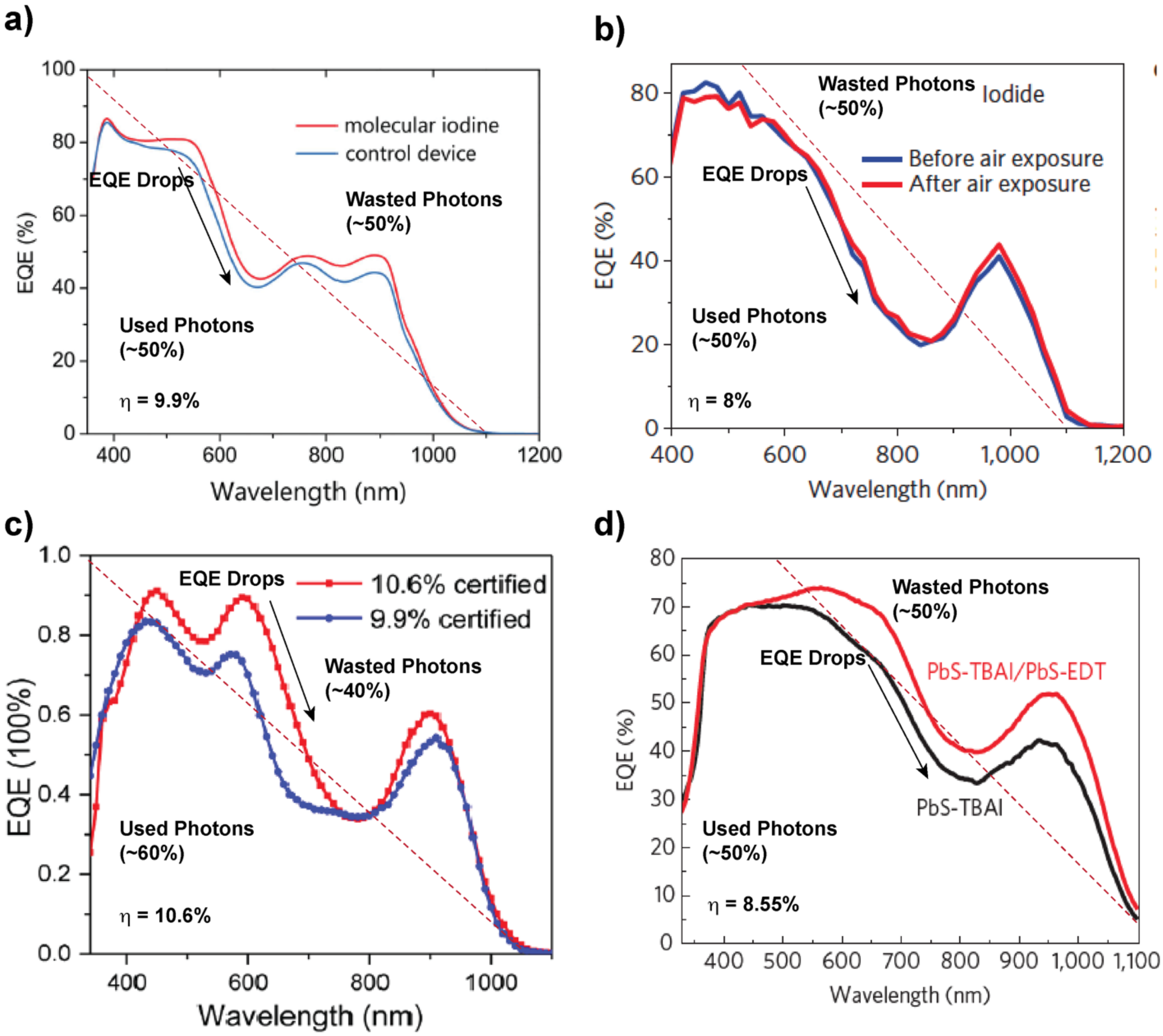

Figure 4.6 Limitations and opportunities towards 20% efficiency in QD photovoltaics. Quantum efficiency for recent QD photovoltaic devices from literatures, a)[146] b)[27] c)[101]d)[100], showing all of them drastic drop in EQE around λ ~600-700 nm. The area under the curve presents photons used and the area over the curve represents photons wasted.

In conclusion, we have presented a technology based on intercalated graphene electrodes to break the restriction that the short diffusion length of QDs imposes in their thickness, which results in poor light absorption towards the infrared. This technology enables strong and uniform EQE in the $\lambda = 600\text{-}950$ nm range. The intercalated configuration herein presented has a direct application to improve broadband spectrum detection towards the infrared using Gr/QD. It also offers a potential path forward for intercalated photovoltaic devices by integrating QDs with n- and p-type layers to separate electrons and holes. Intercalated photovoltaic devices with 1 μm thick QD films could achieve high and uniform QE across the $\lambda = 400\text{-}1000$ nm range to boost QD photovoltaic conversion efficiencies towards 20%. This intercalated technology is not restricted to QDs, it can also be expanded to improve the performance of optoelectronic devices using low-cost materials such as organic molecules, polymers, amorphous materials, or any other material that offers strong light absorption but has short diffusion length.

Chapter 4, in full, is a reprint of the material as it appears in “Near Full Light Absorption and Full Charge Collection in 1-micron Thick Quantum Dot Photodetector Using Intercalated Graphene Monolayer Electrodes” Chen, Wenjun; Ahn, Seungbae; Balingit, Marquez; Wang, Jiaying; Lockett, Malcolm: Vazquez-Mena, Oscar. Submitted. The dissertation author was the primary investigator and author of this paper.

Chapter 5 Conclusion and Future Work

5.1 Conclusions

The objective of this current research is to develop an architecture to overcome the compromise between light absorption and charge extraction caused by QDs short diffusion length in QDs optoelectronic devices. This novel intercalated Gr/QDs structure was developed for quantum dots but is not limited to quantum dots system, it could be applied to any light absorbers, for instance, perovskite or amorphous Si. Especially, materials with short diffusion length would benefit most from this configuration. Graphene could also be alternated with other 2D materials for being charge collectors, such as MoS_2 and other transition metal dichalcogenides (TMDs).

We have successfully achieved layer-by-layer intercalating graphene in QDs films, this architecture shows enhanced performance compared to conventional QDs devices, producing higher EQE across the spectrum as the thickness is increased. The intercalating graphene layers ensure efficient charge collection despite the total thickness, breaking the limitation that diffusion length imposes on practical film thickness.

The role of Gr and QDs play both in charge extraction and in the collection of photogenerated carriers were studied individually. We have studied the evolution of light absorption, photocurrent and conductivity in intercalated film as successive Gr and QD layers are added, allowing to analyze the individual role in the optoelectronic response of the devices. Photoluminescence lifetime were also measured, giving shorter lifetimes for intercalated devices, showing faster charge separation and collection for intercalated devices, charge transport between Gr and QDs was also studied. Furthermore, we also optimized the interspace distance between Gr layers in the intercalated devices. Large interspace facilitates making thicker QDs films with strong light absorption, however this would compromise the charge collection due to short diffusion length of carriers. The interspacing of graphene at 100 nm gives the best performance by considering of this compromise. Moreover, vertical interconnect access (VIAs) gold electrodes were added to intercalated configuration, ensuring the connection with each Gr layer to improve the current collection from all graphene layer and overcome the poor vertical conductivity inside the quantum dots. By utilizing this VIAs with optimized graphene interspacing intercalated structure, we achieved 1-micron meter thick QDs films maintaining 90% quantum efficiency across the whole absorption spectrum.

5.2 Future Work

This intercalated configuration could be applied to other materials system for enhanced charge collection. For PbS QDs system, this intercalated architecture could also be utilized into photovoltaic devices for enhanced power conversion efficiency. Moreover, it could also be applied to CMOS camera for both visible and infrared imaging.

5.2.1 Multi-color Photodetection

Current multi-band photodetector is usually based on single-color detector forming a plane array, multispectral sensing is attractive due to the growing need to extract coincident spectral information to provide better object identification by processing signals from different wavebands. This intercalated architecture is providing a direct path to build multi-color sensor with low-cost fabrication.

In order to achieve a multi-color photodetector, we can take advantages of this intercalated devices by employing different sizes of QDs into different layers. Instead of vertical interconnected gold electrodes being deposited at the same position, gold electrodes could be circumferentially distributed with the center of the device active area. Different sizes of QDs aiming at different photon energy absorption with graphene and gold electrodes can be treated as an individual photodetector, by vertically assembling these photodetectors at a rotated angel, a vertical multi-color photodetector could be achieved.

5.2.2 Photovoltaic

Another meaningful but more challenging path forward is to apply the intercalated architecture to solar cells, by intercalating QDs with n- and p-type intercalated charge collection layers, such as MoS_2 (n-type)[117,123] and Gr (p-type), allowing to separate both electrons and holes to obtain a photovoltaic cell. State-of-the-art solar cells (t ~250 nm) from leading groups in QDs typically show high EQE~80% in the λ ~400−700 nm range, with strong decline to 50% in the λ ~700−1000 nm range as discussed in the chapter 4. This means that about 50-40% of the total incident photons in the λ ~400−1000 nm range are not captured, mainly in the λ ~700−1000 nm range.

Improving EQE to ~95% in the entire λ ~400−1000 nm range would represent collecting almost the entire sunlight photon influx above the bandgap, potentially boosting the photovoltaic performance of QD solar cells from the current 10-15% range[100−102,145] towards 20%. 1-micron thick QDs films with intercalated electrodes represent a potential path forward to achieve 20% efficiencies with QD solar cells.

5.2.3 CMOS-Camera

The intercalated configuration herein presented has a direct application to improve broadband spectrum detection towards the infrared using Gr/QD. Recently, the integration of Gr/QD with CMOS has shown the power of this hybrid technology for broad spectrum imaging.[144] In order to push Gr/QD/CMOS detection technology towards longer wavelengths with deeper penetration depths, thicker QD films can be required, in which case, intercalated films can be the perfect tool to improve photon capture keeping charge collection.

Bibliography

[1] R. Saran, R. J. Curry, *Nat. Photonics* **2016**, *10*, 81.

[2] X. Lan, S. Masala, E. H. Sargent, *Nat. Mater.* **2014**, *13*, 233.

[3] A. De Iacovo, C. Venettacci, L. Colace, L. Scopa, S. Foglia, *Sci. Rep.* **2016**, *6*, 37913.

[4] C. R. Kagan, E. Lifshitz, E. H. Sargent, D. V. Talapin, *Science (80-.).* **2016**, *353*, aac5523.

[5] M. Soreni-Harari, N. Yaacobi-Gross, D. Steiner, A. Aharoni, U. Banin, O. Millo, N. Tessler, *Nano Lett.* **2008**, *8*, 678.

[6] X. Lan, O. Voznyy, F. P. Garcia De Arquer, M. Liu, J. Xu, A. H. Proppe, G. Walters, F. Fan, H. Tan, M. Liu, Z. Yang, S. Hoogland, E. H. Sargent, *Nano Lett.* **2016**, *16*, 4630.

[7] K. Whitham, J. Yang, B. H. Savitzky, L. F. Kourkoutis, F. Wise, T. Hanrath, *Nat. Mater.* **2016**, *15*, 557.

[8] Y. Liu, M. Gibbs, J. Puthussery, S. Gaik, R. Ihly, H. W. Hillhouse, M. Law, *Nano Lett.* **2010**, *10*, 1960.

[9] W. Liu, J. S. Lee, D. V. Talapin, *J. Am. Chem. Soc.* **2013**, *135*, 1349.

[10] C. S. S. Sandeep, J. M. Azpiroz, W. H. Evers, S. C. Boehme, I. Moreels, S. Kinge, L. D. A. Siebbeles, I. Infante, A. J. Houtepen, *ACS Nano* **2014**, *8*, 11499.

[11] M. Scheele, J. H. Engel, V. E. Ferry, D. Hanifi, Y. Liu, A. P. Alivisatos, *ACS Nano* **2013**, *7*, 6774.

[12] B. A. Timp, X. Y. Zhu, *Surf. Sci.* **2010**, *604*, 1335.

[13] F. W. Wise, *Acc. Chem. Res.* **2000**, *33*, 773.

[14] G. H. Carey, A. L. Abdelhady, Z. Ning, S. M. Thon, O. M. Bakr, E. H. Sargent, *Chem. Rev.* **2015**, *115*, 12732.

[15] O. Voznyy, B. R. Sutherland, A. H. Ip, D. Zhitomirsky, E. H. Sargent, *Nat. Rev. Mater.* **2017**, *2*, 17026.

[16] G. Juška, M. Viliunas, K. Arlauskas, N. Nekrašas, N. Wyrsch, L. Feitknecht, *J. Appl. Phys.* **2001**, *89*, 4971.

[17] K. W. Johnston, A. G. Pattantyus-Abraham, J. P. Clifford, S. H. Myrskog, S. Hoogland, H. Shukla, E. J. D. Klem, L. Levina, E. H. Sargent, *Appl. Phys. Lett.* **2008**, *92*, 1.

[18] K. Katsiev, A. H. Ip, A. Fischer, I. Tanabe, X. Zhang, A. R. Kirmani, O. Voznyy, L. R. Rollny, K. W. Chou, S. M. Thon, G. H. Carey, X. Cui, A. Amassian, P. Dowben, E. H. Sargent, O. M. Bakr, *Adv. Mater.* **2014**, *26*, 937.

[19] P. Stadler, B. R. Sutherland, Y. Ren, Z. Ning, A. Simchi, S. M. Thon, S. Hoogland, E. H. Sargent, *ACS Nano* **2013**, *7*, 5757.

[20] Z. Li, F. Gao, N. C. Greenham, C. R. McNeill, *Adv. Funct. Mater.* **2011**, *21*, 1419.

[21] L. Sun, J. J. Choi, D. Stachnik, A. C. Bartnik, B. R. Hyun, G. G. Malliaras, T. Hanrath, F. W. Wise, *Nat. Nanotechnol.* **2012**, *7*, 369.

[22] E. Talgorn, Y. Gao, M. Aerts, L. T. Kunneman, J. M. Schins, T. J. Savenije, M. A. Van Huis, H. S. J. Van Der Zant, A. J. Houtepen, L. D. A. Siebbeles, *Nat. Nanotechnol.* **2011**, *6*, 733.

[23] J. Tang, K. W. Kemp, S. Hoogland, K. S. Jeong, H. Liu, L. Levina, M. Furukawa, X. Wang, R. Debnath, D. Cha, K. W. Chou, A. Fischer, A. Amassian, J. B. Asbury, E. H. Sargent, *Nat. Mater.* **2011**, *10*, 765.

[24] S. J. Oh, N. E. Berry, J. H. Choi, E. A. Gaulding, T. Paik, S. H. Hong, C. B. Murray, C. R. Kagan, *ACS Nano* **2013**, *7*, 2413.

[25] A. H. Ip, S. M. Thon, S. Hoogland, O. Voznyy, D. Zhitomirsky, R. Debnath, L. Levina, L. R. Rollny, G. H. Carey, A. Fischer, K. W. Kemp, I. J. Kramer, Z. Ning, A. J. Labelle, K. W. Chou, A. Amassian, E. H. Sargent, *Nat. Nanotechnol.* **2012**, *7*, 577.

[26] Z. Ning, Y. Ren, S. Hoogland, O. Voznyy, L. Levina, P. Stadler, X. Lan, D. Zhitomirsky, E. H. Sargent, *Adv. Mater.* **2012**, *24*, 6295.

[27] Z. Ning, O. Voznyy, J. Pan, S. Hoogland, V. Adinolfi, J. Xu, M. Li, A. R. Kirmani, J. P. Sun, J. Minor, K. W. Kemp, H. Dong, L. Rollny, A. Labelle, G. Carey, B. Sutherland, I. Hill, A. Amassian, H. Liu, J. Tang, O. M. Bakr, E. H. Sargent, *Nat. Mater.* **2014**, *13*, 822.

[28] D. Bozyigit, M. Jakob, O. Yarema, V. Wood, *ACS Appl. Mater. Interfaces* **2013**, *5*, 2915.

[29] D. Bozyigit, S. Volk, O. Yarema, V. Wood, *Nano Lett.* **2013**, *13*, 5284.

[30] J. E. Mahan, T. W. Ekstedt, R. I. Frank, R. Kaplow, *IEEE Trans. Electron Devices* **1979**, *26*, 733.

[31] A. Zaban, M. Greenshtein, J. Bisquert, *ChemPhysChem* **2003**, *4*, 859.

[32] K. W. Johnston, A. G. Pattantyus-Abraham, J. P. Clifford, S. H. Myrskog, S. Hoogland, H. Shukla, E. J. D. Klem, L. Levina, E. H. Sargent, *Appl. Phys. Lett.* **2008**, *92*, DOI

10.1063/1.2896295.

[33] D. Zhitomirsky, O. Voznyy, S. Hoogland, E. H. Sargent, **2013**, 5282.

[34] G. H. Carey, L. Levina, R. Comin, O. Voznyy, E. H. Sargent, *Adv. Mater.* **2015**, 3325.

[35] E. H. Sargent, *Nat. Photonics* **2012**, *6*, 133.

[36] G. I. Koleilat, L. Levina, H. Shukla, S. H. Myrskog, S. Hinds, A. G. Pattantyus-abraham, E. H. Sargent, *ACS Nano* **2008**, *2*, 833.

[37] W. Shockley, H. J. Queisser, *J. Appl. Phys.* **1961**, *32*, 510.

[38] J. Tang, E. H. Sargent, *Adv. Mater.* **2011**, *23*, 12.

[39] O. E. Semonin, O. E. Semonin, J. M. Luther, S. Choi, H. Chen, J. Gao, A. J. Nozik, M. C. Beard, **2011**, *1530*, 1530.

[40] X. Huang, S. Han, W. Huang, X. Liu, *Chem. Soc. Rev.* **2013**, *42*, 173.

[41] J. M. Luther, M. Law, M. C. Beard, Q. Song, M. O. Reese, R. J. Ellingson, A. J. Nozik, *Nano Lett.* **2008**, *8*, 3488.

[42] W. Ma, S. L. Swisher, T. Ewers, J. Engel, V. E. Ferry, H. A. Atwater, A. P. Alivisatos, *ACS Nano* **2011**, *5*, 8140.

[43] Y. Zhang, D. J. Hellebusch, N. D. Bronstein, C. Ko, D. F. Ogletree, M. Salmeron, A. P. Alivisatos, *Nat. Commun.* **2016**, *7*, 11924.

[44] G. Konstantatos, E. H. Sargent, *Nat. Nanotechnol.* **2010**, *5*, 391.

[45] F. H. L. Koppens, T. Mueller, P. Avouris, A. C. Ferrari, M. S. Vitiello, M. Polini, *Nat. Nanotechnol.* **2014**, *9*, 780.

[46] V. Sukhovatkin, S. Hinds, L. Brzozowski, E. H. Sargent, *Science (80-.).* **2009**, *324*, 1542.

[47] R. Saran, R. J. Curry, *Nat. Photonics* **2016**, *10*, 81.

[48] G. Sargent, Edward H; Konstantatos, *Proc. IEEE* **2009**, *97*.

[49] S. A. McDonald, P. W. Cyr, L. Levina, E. H. Sargent, *Appl. Phys. Lett.* **2004**, *85*, 2089.

[50] G. Konstantatos, L. Levina, A. Fischer, E. H. Sargent, *Nano Lett.* **2008**, *8*, 1446.

[51] S. Hinds, L. Levina, E. J. D. Klem, G. Konstantatos, V. Sukhovatkin, E. H. Sargent, *Adv. Mater.* **2008**, *20*, 4398.

[52] G. Konstantatos, I. Howard, A. Fischer, S. Hoogland, J. Clifford, E. Klem, L. Levina, E.

H. Sargent, *Nature* **2006**, *442*, 180.

[53] G. Konstantatos, J. Clifford, L. Levina, E. H. Sargent, *Nat. Photonics* **2007**, *1*, 531.

[54] J. P. Clifford, G. Konstantatos, K. W. Johnston, S. Hoogland, L. Levina, E. H. Sargent, *Nat. Nanotechnol.* **2009**, *4*, 40.

[55] G. D. B. E. L. Dereniak, *Infrared Detectors and Systems*, **1996**.

[56] N. V. Lavrik, P. G. Datskos, **n.d.**, 145.

[57] R. L. Petritz, *Phys. Rev.* **1956**, *104*, 1508.

[58] G. Konstantatos, M. Badioli, L. Gaudreau, J. Osmond, M. Bernechea, F. P. G. de Arquer, F. Gatti, F. H. L. Koppens, *Nat. Nanotechnol.* **2012**, *7*, 363.

[59] S. P. McGlynn, *Concepts in Photoconductivity and Allied Problems*, **1964**.

[60] S. Espevik, *Mechanism of Photoconductivity in Chemically Deposited Lead Sulfide Layers*, **1971**.

[61] R. Bube, C. T. Ho, *Laser Saturation of Photoconductivity and Determination of Imperfection Parameters in Sensitive Photoconductors*, **1966**.

[62] P. Nagpal, V. I. Klimov, *Nat. Commun.* **2011**, *2*, 486.

[63] L. Turyanska, O. Makarovsky, S. A. Svatek, P. H. Beton, C. J. Mellor, A. Patanè, L. Eaves, N. R. Thomas, M. W. Fay, A. J. Marsden, N. R. Wilson, *Adv. Electron. Mater.* **2015**, *1*, 1.

[64] D. Zhang, L. Gan, Y. Cao, Q. Wang, L. Qi, X. Guo, *Adv. Mater.* **2012**, *24*, 2715.

[65] Y. Q. Huang, R. J. Zhu, N. Kang, J. Du, H. Q. Xu, *Appl. Phys. Lett.* **2013**, *103*, DOI 10.1063/1.4824113.

[66] D. Kufer, I. Nikitskiy, T. Lasanta, G. Navickaite, F. H. L. Koppens, G. Konstantatos, *Adv. Mater.* **2015**, *27*, 176.

[67] D. Zhitomirsky, O. Voznyy, L. Levina, S. Hoogland, K. W. Kemp, A. H. Ip, S. M. Thon, E. H. Sargent, *Nat. Commun.* **2014**, *5*, 1.

[68] X. Lan, S. Masala, E. H. Sargent, *Nat. Mater.* **2014**, *13*, 233.

[69] J. Tang, E. H. Sargent, *Adv. Mater.* **2011**, *23*, 12.

[70] B. Niesen, B. P. Rand, P. Van Dorpe, D. Cheyns, L. Tong, A. Dmitriev, P. Heremans,

Adv. Energy Mater. **2013**, *3*, 145.

[71] V. E. Ferry, M. A. Verschuuren, H. B. T. Li, E. Verhagen, R. J. Walters, R. E. I. Schropp, H. A. Atwater, A. Polman, *Opt. Express* **2010**, *18*, A237.

[72] U. W. Paetzold, E. Moulin, D. Michaelis, W. Böttler, C. Wächter, V. Hagemann, M. Meier, R. Carius, U. Rau, *Appl. Phys. Lett.* **2011**, *99*, 1.

[73] P. W. Flanigan, A. E. Ostfeld, Z. Ye, N. G. Serrino, A. Plummer, D. Pacifici, *2012 Lester Eastman Conf. High Perform. Devices, LEC 2012* **2012**, *113112*, 2009.

[74] D. H. Wang, J. Seifter, J. H. Park, D. G. Choi, A. J. Heeger, *Adv. Energy Mater.* **2012**, *2*, 1319.

[75] I.-K. Ding, J. Zhu, W. Cai, S.-J. Moon, N. Cai, P. Wang, S. M. Zakeeruddin, M. Grätzel, M. L. Brongersma, Y. Cui, M. D. McGehee, *Adv. Energy Mater.* **2011**, *1*, 52.

[76] S. Y. Chou, W. Ding, *Opt. Express* **2013**, *21*, A60.

[77] N. N. Lal, B. F. Soares, J. K. Sinha, F. Huang, S. Mahajan, P. N. Bartlett, N. C. Greenham, J. J. Baumberg, *Opt Express* **2011**, *19*, 11256.

[78] J. Zhu, C. M. Hsu, Z. Yu, S. Fan, Y. Cui, *Nano Lett.* **2010**, *10*, 1979.

[79] F. J. Beck, A. Stavrinadis, S. L. Diedenhofen, T. Lasanta, G. Konstantatos, *ACS Photonics* **2014**, *1*, 1197.

[80] T. Mueller, F. Xia, P. Avouris, *Nat. Photonics* **2010**, *4*, 297.

[81] F. Bonaccorso, Z. Sun, T. Hasan, A. C. Ferrari, *Nat. Photonics* **2010**, *4*, 611.

[82] A. C. Ferrari, F. Bonaccorso, V. Fal'ko, K. S. Novoselov, S. Roche, P. Bøggild, S. Borini, F. H. L. Koppens, V. Palermo, N. Pugno, J. A. Garrido, R. Sordan, A. Bianco, L. Ballerini, M. Prato, E. Lidorikis, J. Kivioja, C. Marinelli, T. Ryhänen, A. Morpurgo, J. N. Coleman, V. Nicolosi, L. Colombo, A. Fert, M. Garcia-Hernandez, A. Bachtold, G. F. Schneider, F. Guinea, C. Dekker, M. Barbone, Z. Sun, C. Galiotis, A. N. Grigorenko, G. Konstantatos, A. Kis, M. Katsnelson, L. Vandersypen, A. Loiseau, V. Morandi, D. Neumaier, E. Treossi, V. Pellegrini, M. Polini, A. Tredicucci, G. M. Williams, B. Hee Hong, J.-H. Ahn, J. Min Kim, H. Zirath, B. J. van Wees, H. van der Zant, L. Occhipinti, A. Di Matteo, I. A. Kinloch, T. Seyller, E. Quesnel, X. Feng, K. Teo, N. Rupesinghe, P. Hakonen, S. R. T. Neil, Q. Tannock, T. Löfwander, J. Kinaret, *Nanoscale* **2015**, *7*, 4598.

[83] Z. Sun, T. Hasan, F. Torrisi, D. Popa, G. Privitera, F. Wang, F. Bonaccorso, D. M. Basko, A. C. Ferrari, **2010**, *4*, 803.

[84] F. H. L. Koppens, D. E. Chang, F. J. García De Abajo, *Nano Lett.* **2011**, *11*, 3370.

[85] A. N. Grigorenko, M. Polini, K. S. Novoselov, *Nat. Photonics* **2012**, *6*, 749.

[86] J. Park, C. Ruiz-vargas, **2009**, 16.

[87] M. Beckmann, D. Parker, D. P. Enot, E. Duval, J. Draper, *Nat. Protoc.* **2008**, *3*, 486.

[88] F. Xia, T. Mueller, R. Golizadeh-mojarad, Y. Lin, J. Tsang, V. Perebeinos, P. Avouris, F. Xia, T. Mueller, R. Golizadeh-mojarad, M. Freitag, **2009**, 0.

[89] F. Xia, T. Mueller, Y. M. Lin, A. Valdes-Garcia, P. Avouris, *Nat. Nanotechnol.* **2009**, *4*, 839.

[90] 1 A K Geim K. S. Novoselov 1* S. V. Morozov,2 D. Jiang,1 Y. Zhang,1 S. V. Dubonos,2 I. V. Grigorieva,1 A. A. Firsov2, *Science (80-.).* **2004**, *306*, 666.

[91] Z. Sun, Z. Liu, J. Li, G. A. Tai, S. P. Lau, F. Yan, *Adv. Mater.* **2012**, *24*, 5878.

[92] J. S. Lee, M. V. Kovalenko, J. Huang, D. S. Chung, D. V. Talapin, *Nat. Nanotechnol.* **2011**, *6*, 348.

[93] I. Nikitskiy, S. Goossens, D. Kufer, T. Lasanta, G. Navickaite, F. H. L. Koppens, G. Konstantatos, *Nat. Commun.* **2016**, *7*, 11954.

[94] D. Kufer, I. Nikitskiy, T. Lasanta, G. Navickaite, F. H. L. Koppens, G. Konstantatos, *Adv. Mater.* **2015**, *27*, 176.

[95] Q. H. Wang, K. Kalantar-Zadeh, A. Kis, J. N. Coleman, M. S. Strano, *Nat. Nanotechnol.* **2012**, *7*, 699.

[96] K. S. Novoselov, D. Jiang, F. Schedin, T. J. Booth, V. V. Khotkevich, S. V. Morozov, A. K. Geim, *Proc. Natl. Acad. Sci.* **2005**, *102*, 10451.

[97] B. Radisavljevic, A. Kis, *Nat. Mater.* **2013**, *12*, 815.

[98] X. Lan, S. Masala, E. H. Sargent, *Nat Mater* **2014**, *13*, 233.

[99] D. Zhitomirsky, O. Voznyy, S. Hoogland, E. H. Sargent, *ACS Nano* **2013**, 5282.

[100] C.-H. M. Chuang, P. R. Brown, V. Bulović, M. G. Bawendi, *Nat. Mater.* **2014**, *13*, 796.

[101] X. Lan, O. Voznyy, F. P. García De Arquer, M. Liu, J. Xu, A. H. Proppe, G. Walters, F. Fan, H. Tan, M. Liu, Z. Yang, S. Hoogland, E. H. Sargent, *Nano Lett.* **2016**, *16*, 4630.

[102] A. Stavrinadis, S. Pradhan, P. Papagiorgis, G. Itskos, G. Konstantatos, *ACS Energy Lett.* **2017**, *2*, 739.

[103] X. Lan, O. Voznyy, A. Kiani, F. P. García De Arquer, A. S. Abbas, G. H. Kim, M. Liu, Z. Yang, G. Walters, J. Xu, M. Yuan, Z. Ning, F. Fan, P. Kanjanaboos, I. Kramer, D. Zhitomirsky, P. Lee, A. Perelgut, S. Hoogland, E. H. Sargent, *Adv. Mater.* **2016**, *28*, 299.

[104] G. Konstantatos, M. Badioli, L. Gaudreau, J. Osmond, M. Bernechea, F. P. G. De Arquer, F. Gatti, F. H. L. Koppens, *Nat. Nanotechnol.* **2012**, *7*, 363.

[105] A. S. Goossens, G. Navickaite, C. Monasterio, S. Gupta, *Nat. Photonics* **2017**, *11*, 366.

[106] Y. Zhang, M. Cao, X. Song, J. Wang, Y. Che, H. Dai, X. Ding, G. Zhang, J. Yao, *J. Phys. Chem. C* **2015**, *119*, 21739.

[107] X. Song, Y. Zhang, H. Zhang, Y. Yu, M. Cao, Y. Che, H. Dai, J. Yang, X. Ding, J. Yao, *Nanotechnology* **2017**, *28*, DOI 10.1088/1361-6528/aa5faf.

[108] S. Bae, H. Kim, Y. Lee, X. Xu, J. S. Park, Y. Zheng, J. Balakrishnan, T. Lei, H. Ri Kim, Y. Il Song, Y. J. Kim, K. S. Kim, B. Özyilmaz, J. H. Ahn, B. H. Hong, S. Iijima, *Nat. Nanotechnol.* **2010**, *5*, 574.

[109] X. Li, W. Cai, J. An, S. Kim, J. Nah, D. Yang, R. Piner, A. Velamakanni, I. Jung, E. Tutuc, S. K. Banerjee, L. Colombo, R. S. Ruoff, *Science (80-.).* **2009**, *324*, 1312.

[110] R. X. He, P. Lin, Z. K. Liu, H. W. Zhu, X. Z. Zhao, H. L. W. Chan, F. Yan, *Nano Lett.* **2012**, *12*, 1404.

[111] Y. Fu, H. Xu, S. Bai, D. Qiu, J. Sun, Z. Wang, X. Zhang, *Macromol. Rapid Commun.* **2002**, 256.

[112] M. Shimomura, T. Sawadaishi, *Curr. Opin. Colloid Interface Sci.* **2001**, *6*, 11.

[113] T. Cassagneau, T. E. Mallouk, J. H. Fendler, *J. Am. Chem. Soc.* **1998**, *120*, 7848.

[114] A. R. Kirmani, G. H. Carey, M. Abdelsamie, B. Yan, D. Cha, L. R. Rollny, X. Cui, E. H. Sargent, A. Amassian, *Adv. Mater.* **2014**, *26*, 4717.

[115] P. Maraghechi, A. J. Labelle, A. R. Kirmani, X. Lan, M. M. Adachi, S. M. Thon, S. Hoogland, A. Lee, Z. Ning, A. Fischer, A. Amassian, E. H. Sargent, *ACS Nano* **2013**, *7*, 6111.

[116] I. Nikitskiy, S. Goossens, D. Kufer, T. Lasanta, G. Navickaite, F. H. L. Koppens, G. Konstantatos, *Nat. Commun.* **2016**, *7*, 11954.

[117] D. Kufer, I. Nikitskiy, T. Lasanta, G. Navickaite, F. H. L. Koppens, G. Konstantatos, *Adv. Mater.* **2014**, n/a.

[118] F. Yan, J. Li, S. M. Mok, *J. Appl. Phys.* **2009**, *106*, DOI 10.1063/1.3225760.

[119] D. Kufer, G. Konstantatos, *ACS Photonics* **2016**, *3*, 2197.

[120] S. D. Stranks, G. E. Eperon, G. Grancini, C. Menelaou, M. J. P. Alcocer, T. Leijtens, L. M. Herz, A. Petrozza, H. J. Snaith, *Science (80-.).* **2013**, *342*, 341.

[121] G. Xing, N. Mathews, S. Sun, S. S. Lim, Y. M. Lam, M. Graẗzel, S. Mhaisalkar, T. C. Sum, *Science (80-.).* **2013**, *342*, 344.

[122] A. Stavrinadis, S. Pradhan, P. Papagiorgis, G. Itskos, G. Konstantatos, *ACS Energy Lett.* **2017**, *2*, 739.

[123] D. Kufer, T. Lasanta, M. Bernechea, F. H. L. Koppens, G. Konstantatos, *ACS Photonics* **2016**, *3*, 1324.

[124] W. Chen, J. Castro, S. Ahn, X. Li, O. Vazquez-Mena, *Adv. Mater.* **2019**, *31*, 1.

[125] E. Sargent, *Nat. Photonics* **2012**, *6*, 133.

[126] W. van der G. Van Der Wiel, S. De Franceschi, W. van der Wiel, S. De Franceschi, J. Elzerman, T. Fujisawa, S. Tarucha, L. Kouwenhoven, *Rev. Mod. Phys.* **2002**, *75*, 1.

[127] C. R. Kagan, C. B. Murray, *Nat. Nanotechnol.* **2015**, *10*, 1013.

[128] N. Huo, G. Konstantatos, *Adv. Mater.* **2018**, *30*, 1.

[129] W. Chen, J. Castro, S. Ahn, X. Li, O. Vazquez-Mena, *Adv. Mater.* **2019**, *1807894*, 1807894.

[130] R. X. He, P. Lin, Z. K. Liu, H. W. Zhu, X. Z. Zhao, H. L. W. Chan, F. Yan, *Nano Lett.* **2012**, *12*, 1404.

[131] G. Tai, F. Yan, Z. Liu, J. Li, Z.-H. Sun, S.-P. Lau, *ACS Nano* **2011**, *6*, 810.

[132] A. K. Rath, M. Bernechea, L. Martinez, G. Konstantatos, *Adv. Mater.* **2011**, *23*, 3712.

[133] D. Zhitomirsky, O. Voznyy, S. Hoogland, E. H. Sargent, *ACS Nano* **2013**, *7*, 5282.

[134] G. Konstantatos, M. Badioli, L. Gaudreau, J. Osmond, M. Bernechea, F. P. G. de Arquer, F. Gatti, F. H. L. Koppens, *Nat. Nanotechnol.* **2012**, *7*, 363.

[135] F. Yan, J. Li, S. M. Mok, *J. Appl. Phys.* **2009**, *106*, DOI 10.1063/1.3225760.

[136] W. Chen, S. Ahn, C. Rangel, O. Vazquez-Mena, *Front. Mater.* **2019**, *6*, 1.

[137] Z. S. Hosseini, H. A. Bafrani, A. Naseri, A. Z. Moshfegh, *Appl. Surf. Sci.* **2019**, *483*,

1110.

[138] Y. H. Zhou, H. N. An, C. Gao, Z. Q. Zheng, B. Wang, *Mater. Lett.* **2019**, *237*, 298.

[139] J. M. Luther, M. Law, M. C. Beard, Q. Song, M. O. Reese, R. J. Ellingson, A. J. Nozik, *Nano Lett.* **2008**, *8*, 3488.

[140] H. Lu, G. M. Carroll, N. R. Neale, M. C. Beard, *ACS Nano* **2019**, *13*, 939.

[141] R. A. Taylor, K. Ramasamy, *SPR Nanosci.* **2017**, *4*, 142.

[142] G. Zhai, A. Bezryadina, A. J. Breeze, D. Zhang, G. B. Alers, S. A. Carter, *Appl. Phys. Lett.* **2011**, DOI 10.1063/1.3617469.

[143] W. Gao, G. Zhai, C. Zhang, Z. Shao, L. Zheng, Y. Zhang, Y. Yang, X. Li, X. Liu, B. Xu, *RSC Adv.* **2018**, DOI 10.1039/c8ra01422a.

[144] S. Goossens, G. Navickaite, C. Monasterio, S. Gupta, J. J. Piqueras, R. Pérez, G. Burwell, I. Nikitskiy, T. Lasanta, T. Galán, E. Puma, A. Centeno, A. Pesquera, A. Zurutuza, G. Konstantatos, F. Koppens, *Nat. Photonics* **2017**, *11*, 366.

[145] E. M. Sanehira, A. R. Marshall, J. A. Christians, S. P. Harvey, P. N. Ciesielski, L. M. Wheeler, P. Schulz, L. Y. Lin, M. C. Beard, J. M. Luther, *Sci. Adv.* **2017**, *3*, eaao4204.

[146] X. Lan, O. Voznyy, A. Kiani, F. P. García De Arquer, A. S. Abbas, G. H. Kim, M. Liu, Z. Yang, G. Walters, J. Xu, M. Yuan, Z. Ning, F. Fan, P. Kanjanaboos, I. Kramer, D. Zhitomirsky, P. Lee, A. Perelgut, S. Hoogland, E. H. Sargent, *Adv. Mater.* **2016**, *28*, 299.